

1 **Role of atmospheric aerosols in severe winter fog over Indo Gangetic Plains of India: a**
2 **case study**

3 Chandrakala Bharali¹, Mary Barth², Rajesh Kumar², Sachin D. Ghude³, Vinayak Sinha⁴, Baerbel Sinha⁴

4 ¹ Dibrugarh University, Dibrugarh, Assam, India

5 ² NSF National Centre for Atmospheric Research, Boulder, CO, US

6 ³ Indian Institute of Tropical Meteorology, Ministry of Earth Sciences, Pune, India

7 ⁴ Department of Earth and Environmental Sciences, Indian Institute of Science Education and Research, Mohali,
8 Punjab, India

9 **Correspondence:** chandrakalabharali@gmail.com, barthm@ucar.edu

10

11 **Abstract**

12 Winter fog and severe aerosol loading in the boundary layer over North India, particularly in the Indo-
13 Gangetic Plain (IGP), disrupt daily life of millions of people in the region. To understand better the
14 role of aerosol-radiation feedback on the occurrence, spatial extent, and persistence of winter fog; and
15 the associated aqueous chemistry in fog in the IGP, several model simulations have been performed
16 using the Weather Research and Forecasting model coupled with chemistry (WRF-Chem). While
17 WRF-Chem was able to represent the fog formation for the December 23-24, 2017 fog event over the
18 central IGP in comparison to station and satellite observations, the model underestimated PM_{2.5}
19 concentrations compared to the Central Pollution Control Board of India monitoring network. While
20 evaluating aerosol composition for fog events in IGP, we found that the WRF-Chem aerosol
21 composition was quite different from measurements obtained during the Winter Fog Experiment in
22 Delhi, with secondary aerosols, particularly chloride aerosol fraction being strongly underpredicted
23 (~66.6%). Missing emission sources (e.g., industry and residential burning of cow dung and trash) and
24 aerosol and chemistry processes need to be investigated to improve model-observation agreement. By
25 investigating a fog event on December 23-24, 2017 over central IGP, we found that the aerosol-
26 radiation feedback weakens turbulence, lowers the boundary layer height, and increases PM_{2.5}
27 concentrations and RH within the boundary layer. Factors affecting the feedback include loss of
28 aerosols through deposition of cloud droplets and internal mixing of absorbing and scattering aerosols.
29 Aqueous-phase chemistry increases the PM_{2.5} concentrations, which subsequently affects the aerosol-
30 radiation feedback by both increased mass concentrations and aerosol sizes. With aerosol-radiation
31 interaction and aqueous phase chemistry, fog formation began 1-2 hours earlier and caused a longer
32 fog duration than when these processes were not included in the WRF-Chem simulation. The increase
33 in RH in both the experiments is found to be important for fog formation as it promoted the growth of
34 aerosol size through water uptake, increasing the fog water content over IGP. The results from this

35 study suggest that the aerosol-radiation feedback and secondary aerosol formation play an important
36 role in the air quality and the intensity and lifetime of fog over IGP, yet other feedbacks, such as
37 aerosol-cloud interactions, need to be quantified.

38

39 **1 Introduction**

40 The Indo-Gangetic Plain (IGP; 21°35'-32°28'N latitude. and 73°50'-89°49'E longitude) in the
41 northern part of the Indian subcontinent is one of the most densely populated and heavily polluted
42 regions in South Asia. The rapid population and economic growth in the IGP region over the last
43 decade have increased air pollution over this region. This is evident from the increasing trend in AOD
44 and NO₂ column concentration over India reported in recent studies (Dey and Di Girolamo, 2011;
45 Ghude et al., 2013; Krishna Moorthy et al., 2013), which has slowed and reversed only recently
46 (Sarkar et al., 2019). The high concentration of aerosols along the IGP and their adverse effects on
47 human health and the environment are increasing (Ghude et al., 2016). Consequently, more than 500
48 million people living in the IGP breathe air that exceeds the National Ambient Air Quality Standards
49 (NAAQS), which has reduced the life expectancy of the people (Debnath et al., 2022; Lelieveld et al.,
50 2015). Lelieveld et al., (2015) estimated a very high number of premature deaths (0.716 million per
51 year) linked to aerosols (PM_{2.5}), thus making Southeast Asia one of the largest regions affected by
52 premature mortality globally.

53 One of the major environmental concerns in the IGP is the urban air quality during winter,
54 especially over the mega-cities, e.g., Delhi, located in the north-western part of IGP (Ghude et al.,
55 2020; Jena et al., 2021; Sengupta et al., 2022). Several urban air pollution hotspots along the IGP
56 extend from northwest to east with monthly average PM_{2.5} greater than 200 $\mu\text{g m}^{-3}$ (NAAQS=60 $\mu\text{g m}^{-3}$,
57 24 hr average) in the winter season (Bharali et al., 2019; Krishna et al., 2019). IGP is dominated
58 mainly by fine mode particulates, especially over central to eastern IGP, during post-monsoon and
59 winter (Kumar et al., 2018). Biomass burning (agricultural waste burning, domestic heating, etc.) is an
60 important contributor to the observed high PM_{2.5} loading over IGP during these seasons (Kulkarni et
61 al., 2020; Pant et al., 2015; Pawar and Sinha, 2022; Sharma et al., 2010; Yadav et al., 2020). Delhi is
62 affected substantially by the emissions from agricultural waste burning in the north-western states of
63 Punjab and Haryana during the post-monsoon (October-November) season (Badarinath et al., 2009;
64 Jethva et al., 2018; Kumar et al., 2021). Studies showed that PM_{2.5} increased from ~50 $\mu\text{g m}^{-3}$ to as
65 high as 300 $\mu\text{g m}^{-3}$ (Ojha et al., 2020), and AOD reached 0.98 with the presence of absorbing aerosols
66 (Singh et al., 2018) during the peak biomass burning in post-monsoon.

67 IGP experiences fog (both radiation and advection fog) every winter after the passage of the
68 synoptic wind system called the “Western Disturbances”. The majority of fog events in the IGP during
69 December-January are radiation fog (Deshpande et al., 2023; Ghude et al., 2023), formed due to
70 radiative cooling of the surface. The number of low visibility days due to haze/fog formation has been

71 increasing significantly (Ghude et al., 2017; Jenamani, 2007; Singh and Dey, 2012), impacting socio-
72 economic activities, e.g., aviation (Kulkarni et al., 2019). The increase in the intensity and regional
73 extent of fog over IGP is consistent with the increasing trend in aerosol concentration due to
74 increasing anthropogenic emissions (Sarkar et al., 2006; Syed et al., 2012).

75 Several factors control the formation and persistence of fog in the IGP, e.g., stable boundary
76 layer, low temperature, availability of moisture (supplied by the Western Disturbances and irrigation
77 activities), and the aerosol number and composition (Acharja et al., 2022; Dhangar et al., 2021). It has
78 also been suggested that the atmospheric rivers (moisture incursion from Arabian Sea) act as a source
79 of water vapor over IGP, which fuels the intensification of fog and haze (Verma et al., 2022) during
80 winter. The high aerosol concentration in the boundary layer influences fog formation (Gautam et al.,
81 2007; Safai et al., 2019) over the IGP by providing the needed cloud condensation nuclei (CCN) for
82 activation into fog droplets. In addition, aerosols induce surface cooling by reducing solar radiation at
83 the surface while warming the lower troposphere by absorption (Ding et al., 2016; Yu et al., 2002). A
84 reduction in surface-reaching solar radiation by ~19% has been reported during winter over Kanpur in
85 the IGP (Dey and Tripathi, 2007). The reduced solar flux affects the boundary layer stability and
86 depth by suppressing the thermals and thus further increasing the surface aerosol concentration via
87 aerosol-radiation feedback, which is very strong over the IGP (Bharali et al., 2019). Kumar et al.,
88 (2020) have shown that aerosol-radiation feedback significantly improves the accuracy of PM_{2.5} and
89 temperature forecasts in Delhi. Srivastava et al., (2018) reported that the direct aerosol forcing over
90 polluted regions is very large with values up to $-80.0 \pm 7.2 \text{ W m}^{-2}$ over the IGP in the winter season.

91 Aerosol-radiation interaction determines that the aerosol distribution is critical for the evolution
92 of fog (Bodaballa et al., 2022; Steeneveld et al., 2015), while microphysics is important for fog
93 formation and dispersal (Boutle et al., 2018; Maalick et al., 2016). Although the relationship between
94 the aerosol chemical composition and aerosol activation to CCN has not been fully understood yet,
95 studies have found that the chemical composition and mixing state of aerosols affect the
96 hygroscopicity (κ) of aerosols (Bodaballa et al., 2022; Ma et al., 2013; Moore et al., 2012; Zhang et
97 al., 2014a). Fog processes involve a complex interplay between local meteorology, radiation,
98 microphysics, and aerosol chemistry, making it difficult to understand the fog lifecycle (Acharja et al.,
99 2022; Maalick et al., 2016; Zhang et al., 2014b). There is considerable heterogeneity in the spatial and
100 temporal aerosol properties over IGP and the poor estimates of their mixing state. Therefore,
101 prediction of fog by weather models is still challenging with biases in fog's onset and dispersal
102 timings.

103 Previous studies have focussed on the impacts of meteorological conditions, topography, or
104 anthropogenic emissions on the poor air quality and intensification of fog during winter over IGP (e.g.
105 Hakkim et al., 2019). However, studies on the effect of feedback induced by the aerosols on the
106 meteorological conditions and thus on aerosol concentration are very limited over this region, except
107 for a few above-mentioned studies which discuss how the aerosol-radiation feedback favors haze and

108 fog during winter. Moreover, fog can provide a medium for aqueous-phase reactions. While several
109 earlier studies have reported an increase in secondary aerosols during fog over IGP, a sensitivity study
110 examining the impact of fog on aqueous phase chemistry has not yet been done over IGP.

111 In the present work, we aim to find the suitable chemistry/physics as well as the meteorology
112 initial/boundary conditions that lead to improved simulations of fog events in the Weather Research
113 and Forecasting model coupled with chemistry (WRF-Chem; (Fast et al., 2006; Grell et al., 2005;
114 Powers et al., 2017). We also explore the role of aerosol-radiation feedback on fog properties as the
115 high aerosol loadings in northern India can impact the heating rates, temperature inversions, and
116 boundary layer height. The role of aqueous chemistry on fog properties and vice-versa is also
117 investigated.

118

119 **2 Methodology**

120 Fog formed due to radiative cooling, based on the onset time of fog and low wind speeds (Deshpande
121 et al., 2023 and references therein), at the surface on both 23rd and 24th December 2017 over a
122 widespread region of the IGP (Fig. 1a, b). The fog region is located over an area with high PM_{2.5}
123 anthropogenic emissions (Fig. 1c). The IGP is a large region with varying meteorology and aerosol
124 characteristics, therefore, it is divided into three areas, northwest (NWIGP: latitude-longitude range,
125 27°N-32°N,75°E-79°N), central (CIGP: latitude-longitude range, 25°N-28°N,79°E-83°E), and east
126 (EIGP: latitude-longitude range, 24°N-27°N, 83°E-87°E) which are marked by the black rectangles in
127 Fig.1c. Although biomass burning and anthropogenic emissions dominate throughout the IGP during
128 post-monsoon and winter season, the north-westerly wind system results in the gradient distribution of
129 AOD over this region. The downwind regions, CIGP and EIGP are influenced by the long-range
130 transport from the NWIGP, resulting in high AOD with dominant fine particulates over CIGP and
131 EIGP, especially during post-monsoon and winter (Kedia et al., 2014; Kumar et al., 2018). Therefore,
132 representative stations from each region listed in section 2.2 are considered for the sensitivity
133 analyses.

134

135 **2.1 Modeling**

136 The WRF-Chem model version 4.0.3 is used for this study. Earlier studies have successfully
137 used WRF-Chem to predict fog (Pithani et al., 2019) and in the study of aerosol-radiation feedback on
138 air quality (Kumar et al., 2020; Bharali et al., 2019) and fog (Shao et al., 2023). The model domain is
139 centered at Delhi (77.1°E, 28.7°N) with 300 grid points in the east-west, 170 grid points in the south-
140 north direction (Fig. 1c), and 50 vertical eta levels with the model top at 50 hPa. The horizontal grid
141 spacing of the domain is 10 km, while the vertical grid spacing varies from higher resolution (~200 m)
142 in the boundary layer to coarser resolution (~1200 m) near the model top. We conduct three model
143 configurations (Table 1) for December 20-24, 2017 to identify the best configuration for
144 meteorological simulations. The three experiments have been designed with different combinations of

145 meteorological initial/lateral boundary conditions and planetary boundary layer (PBL) physics.
146 Experiment 1 (EXP1) uses the National Centers for Environmental Predictions (NCEP) Final Analysis
147 (GFS-FNL; $1^\circ \times 1^\circ$, 6 hourly) meteorology data for initial and boundary conditions and the YSU
148 (Yonsei University; (Hong et al., 2006) PBL scheme. Experiments 2 and 3 (EXP2, EXP3) use ERA-
149 Interim Project ($1.125^\circ \times 0.703^\circ$, 6 hourly) for meteorology initial and boundary conditions. EXP2
150 uses the YSU PBL scheme while EXP3 uses the ACM2 (Asymmetric Convective Model version 2)
151 PBL scheme. ACM2, is a hybrid of the original nonlocal closure (Pleim and Chang, 1992) and a local
152 closure eddy diffusion scheme (Pleim, 2007a, 2007b). The YSU PBL option was coupled with the
153 Noah LSM while ACM2 was coupled with Pleim-Xiu LSM. While YSU permits investigations of
154 both aerosol-radiation (AR) and aerosol-cloud interactions (ACI), ACI is not possible when using the
155 ACM2 PBL scheme because in WRF the ACM2 PBL scheme does not provide the exchange
156 coefficient for heat, which is required to calculate the maximum supersaturations and therefore the
157 activation fraction for aerosol mass and number for each bin/mode, which is based on the Abdul-
158 Razzak and Ghan, (2002) scheme. However, ACM2 has been shown to perform well for air quality in
159 the polluted regions (Mohan and Gupta, 2018; Gunwani and Mohan, 2017; Xie et al., 2012, Mohan
160 and Bhati, 2011). Mohan and Gupta (2018) tested the YSU and ACM2 schemes during the summer
161 time (1-15 June 2010) and focused on the evaluation of temperature, wind speed, PBL height, ozone,
162 and PM_{10} . Although these studies recommend using the nonlocal ACM2 PBL scheme for air quality
163 prediction for IGP, there are still seasonal, day-night, and regional biases in the PBL schemes.
164 Gunwani and Mohan (2017) showed that ACM2, QNSE (Quasi Normal Scale Elimination), and MYJ
165 (Mellor-Yamada-Janjić) schemes work well in predicting temperature, humidity, and wind speed in
166 different regions of India. Mohan and Bhati (2011) found that using the ACM2 PBL scheme with
167 Pleim Xiu surface physics improved wintertime meteorology estimates in Delhi indicating its potential
168 in fog predictions, whereas Pithani et al., (2019) recommend using the local PBL scheme MYNN2.5
169 (Mellor-Yamada-Nakanishi-Niino level 2.5). Shin and Hong (2011) found that a non-local (e.g.,
170 ACM2, YSU) scheme is favorable in unstable conditions and a local scheme (e.g., MYJ, Boulac) in
171 stable conditions. All these studies suggest the need for careful consideration of the above-mentioned
172 biases while selecting a PBL scheme. Therefore, to ensure that WRF captures all the relevant
173 meteorological parameters including relative humidity reasonably well during fog events in winter, we
174 designed EXP1, EXP2 and EXP3.

175 The advantage of Pleim-Xiu LSM (PX-LSM) is that it allows nudging of soil moisture and
176 temperature to improve the prediction of meteorology near the surface (Pleim and Gilliam, 2009;
177 Pleim and Xiu, 2003; Xiu and Pleim, 2001) which Noah LSM does not include. The PX-LSM
178 includes two-layer soil (0–1 and 1–100 cm) model, canopy moisture, and aerodynamic and stomatal
179 resistance. Ground surface (1 cm) temperature is calculated from the surface energy balance using a
180 force-restore algorithm for heat exchange within the soil. Although the two-layer approach in PX-
181 LSM is less detailed than the multilayer soil models such as the Noah LSM (four soil layers; Chen and

182 Dudhia 2001), it performs well with realistic initialization for soil moisture and through dynamic
183 adjustment in the model simulation where soil moisture is indirectly nudged according to differences
184 in 2-m temperature (T2) and 2-m relative humidity (RH) between the model and observation (Pleim
185 and Xiu, 2003). Soil moisture nudging adjusts the surface evaporation (direct soil surface evaporation,
186 vegetative evapotranspiration, and evaporation from wet canopies) which then affects the partitioning
187 of available surface energy into latent and sensible heat flux and thus reduces errors in T2 and 2-m
188 RH.

189 For EXP2, meteorological initial conditions were refreshed every 24 hours, while EXP3 was a
190 continuous run but soil moisture was nudged to the Era-Interim dataset to improve the prediction of
191 surface fluxes. All other physics and chemistry options are the same for all the experiments except the
192 surface physics option, which changes with the PBL scheme used. The deposition of cloud droplets is
193 an important moisture and aerosol sink during fog events. For all these simulations, the deposition
194 velocity of cloud droplets was reduced to 0.01 m s^{-1} based on Stoke's Law and previous studies
195 (Katata et al., 2015; Tav et al., 2018) because its default value (0.1 m s^{-1}), is large.

196 To examine the radiative effects of aerosols and aqueous phase chemistry additional
197 simulations have been done using the meteorological configuration in EXP3, with aerosol-radiation
198 (wFB) feedback plus aqueous chemistry (wAq.chem), without aerosol-radiation feedback (nFB) but
199 with aqueous chemistry, and without aqueous chemistry (noAq.chem) but with aerosol-radiation
200 feedback. The analysis has been done for the fog events on 23rd and 24th December 2017 as

$$201 \quad F_{\text{ARF}} = P(\text{wFB-nFB})$$

$$202 \quad F_{\text{Aq.chem}} = P(\text{wAq.chem-noAq.chem})$$

203 where F_{ARF} is the impact due to aerosol radiation feedback on the meteorological parameters/chemical
204 species (P) and $F_{\text{Aq.chem}}$ is the impact due to the inclusion of aqueous phase chemistry

205

206 Emissions used in the WRF-Chem simulations are from the EDGAR-HTAP v2 (*Emissions*
207 *Database for Global Atmospheric Research- Hemispheric Transport of Air Pollution; $0.1^\circ \times 0.1^\circ$)*
208 *inventory for anthropogenic emissions and FINN v2.2 (Fire INventory from NCAR; $1 \text{ km} \times 1 \text{ km}$) fire*
209 *emission inventory* (Wiedinmyer et al., 2011). Trash-burning emissions (Chaudhary et al., 2021) are
210 also included in the simulations. The model calculates the biogenic emissions online using MEGAN
211 v2.04 (*Model of Emissions of Gases and Aerosols from Nature*) (Guenther et al., 2006). The initial and
212 lateral boundary conditions for chemical constituents are from the global chemistry transport model
213 CAM-Chem (*Community Atmosphere Model with Chemistry*) (Emmons et al., 2020).

214 The MOZART (Model for Ozone and Related chemical Tracers) chemical mechanism
215 (Emmons et al., 2010) is used for gas-phase chemistry, which includes 85 gas-phase species, 39
216 photolysis, and 157 gas-phase reactions. It has been updated to include an explicit treatment of
217 aromatic compounds, HONO, C_2H_2 , and isoprene oxidation scheme (Knote et al., 2014). The lumped
218 toluene used by Emmons et al., (2010) has been speciated into benzene, toluene, and lumped isomers

219 of xylenes (Knote et al., 2014). For this study, HCl emissions, transport, dry, and wet deposition are
220 represented. However, HCl gas-phase reaction is not included in MOZART.

221 The Model for Simulating Aerosol Interactions and Chemistry (MOSAIC) with four size bins
222 (0.039–0.156, 0.156–0.625, 0.625–2.500, and 2.5–10.0 μm dry diameters) coupled with MOZART
223 gas-phase chemistry is used (Fast et al., 2006; Zaveri et al., 2008). The bin sizes are defined by their
224 lower and upper dry particle diameters, so there is no transfer of particles between bins during water
225 uptake or loss. It is assumed that aerosols in each bin are internally mixed with the same chemical
226 composition while they are externally mixed in different bins.

227 The aerosol composition includes sulfate (SO_4^{2-}), ammonium (NH_4^+), nitrate (NO_3^-), aerosol
228 water, sea salt (Na^+ , Cl^-), methanesulfonate (CH_3SO_3^-), carbonate (CO_3^{2-}), calcium (Ca^+), black carbon
229 (BC), organic mass (OC), and unspecified inorganic species such as silica, inert minerals, and trace
230 metals lumped together as other inorganic mass (OIN). For OC, primary OC and secondary OC are
231 represented separately, where the latter is simulated using the volatility basis set (VBS) approach.
232 Reactive inorganic species such as potassium (K^+) and magnesium (Mg^+) are usually present in much
233 smaller amounts and are equivalent to Na^+ since their sulfate, nitrate, and chloride salts are similar in
234 terms of their solubility in water.

235 MOSAIC treats condensation and evaporation of trace gases to/from particles, nucleation
236 (new particle formation), and coagulation. Aerosol coagulation (Brownian) is based on (Jacobson et
237 al., 1994) and nucleation is based on (Wexler et al., 1994) parameterization of $\text{H}_2\text{SO}_4\text{-H}_2\text{O}$
238 homogeneous nucleation. Sulfate, nitrate, chloride, and ammonium aerosols are mainly formed
239 through oxidation and neutralization/condensation of gas precursors. Gas-phase sulfuric acid (H_2SO_4)
240 is produced by the gas-phase oxidation of SO_2 by OH and nitric acid (HNO_3) formation is via the
241 oxidation of NO_2 by OH. HCl is a primary emission product. The neutralization/condensation of
242 H_2SO_4 , HCl, and HNO_3 with NH_3 produces ammonium such as ammonium sulfate ($(\text{NH}_4)_2\text{SO}_4$),
243 ammonium bisulfate (NH_4HSO_4), ammonium chloride (NH_4Cl) and ammonium nitrate (NH_4NO_3),
244 respectively. The thermodynamic modules in MOSAIC for the dynamic gas-particle partitioning of
245 aerosols MTEM (Multicomponent Taylor Expansion Method) and MESA (Multicomponent
246 Equilibrium Solver for Aerosols) calculate the activity coefficient in aqueous phase aerosols and
247 compute the intraparticle solid-liquid phase equilibrium respectively (Zaveri et al., 2005, 2008). The
248 Adaptive Step Time-split Euler Method (ASTEM) coupled with MESA-MTEM dynamically
249 integrates the mass transfer equations.

250 Aqueous-phase chemistry uses a bulk water approach employing the Fahey and Pandis (2001)
251 mechanism. It calculates sulfate formation, formaldehyde oxidation, and non-reactive uptake of nitric
252 acid, hydrochloric acid, ammonia, and other trace gases (Chapman et al., 2009; Pye et al., 2020).
253 Aqueous-phase sulfate is produced via oxidation of SO_2 by H_2O_2 , O_3 , TMI (Transition metal Ion:
254 Fe(III), Mn(II)) catalyzed O_2 and NO_2 . TMI concentrations are prescribed in the model to $0.01 \mu\text{g m}^{-3}$
255 for Fe(III) and $0.005 \mu\text{g m}^{-3}$ for Mn(II) (Martin and Good, 1991). The Fe(III) values are within the

256 range of water soluble iron in winter time aerosol reported in India (Kumar and Sarin, 2010). Wet
257 removal (scavenging), is represented by the (Neu and Prather, 2012) scheme for trace gases and Easter
258 et al., (2004) for aerosols.

259

260 **2.2 Observations**

261 To evaluate the model output, observations of aerosols and meteorology have been obtained
262 from several satellites as well as ground-based measurement platforms. To examine the aerosol
263 loading and spatial and temporal distribution, daily Level 2 Aerosol Optical Depth (AOD) retrievals
264 from the Moderate Resolution Imaging Spectroradiometer (MODIS) aboard Terra and Aqua satellites
265 are obtained at the spatial resolution of 10 km x 10 km (at nadir) pixel array. It provides aerosol
266 properties from the Dark Target (DT) algorithm applied over the ocean and dark land (e.g.,
267 vegetation) and Deep Blue (DB) algorithms over the entire land areas, including both dark and bright
268 surfaces. Each MOD04_L2 (Terra) / MYD04_L2 (Aqua) products are available at a 5-minute time
269 interval with an output grid of 135 pixels in width by 203 pixels in length.

270 The Indian National Satellites (INSAT-3D) in the geostationary orbit at inclinations of 82°
271 longitude provide an imager fog product (3DIMG_L2C_FOG) with a spatial resolution of 4 km every
272 30 min (www.mosdac.gov.in). For daytime, the visible channel observation is used to detect fog,
273 whereas thermal infrared is used to reduce false alarms such as medium/high clouds and snow areas.
274 INSAT 3D's 'day microphysics' data component analyzes solar reflectance at three wavelengths: 0.5
275 μm (visible), 1.6 μm (shortwave infrared), and 10.8 μm (thermal infrared). Night-time fog is derived
276 from TIR-1 (12.0 μm and 10.0 μm) and MIR (10.8 μm and 3.9 μm) channel brightness temperature
277 over the Indian region. INSAT-3D provides fog intensity varying from 1 to 4 indicating SHALLOW
278 for visibility > 600 m; MODERATE, DENSE, and VERY_DENSE, respectively for visibility varying
279 from 0 to 500 m (Banerjee and Padmakumari, 2020). If the visibility is greater than 700 m it indicates
280 no fog while visibility > 1000 m represents very clear skies. Validation of INSAT-3D fog products
281 over the IGP shows a 66%-68% probability of detection and a 10% false alarm rate. It also captures
282 the entire life cycle of fog from formation to dissipation. However, detecting fog during multilayer
283 clouds is still challenging with INSAT-3D (Arun et al., 2018; Chaurasia and Gohil, 2015; Chaurasia
284 and Jenamani, 2017).

285 Ground-based monitoring sites provide hourly data of relative humidity, surface temperature,
286 and wind speed measured by the Central Pollution Control Board, CPCB (<http://cpcb.nic.in>). Given
287 the data availability from CPCB stations, nine stations have been considered representing each region
288 of IGP, which include, Amritsar, IGI Airport (Indira Gandhi International Airport, Delhi), IHBAS
289 (Institute of Human Behaviour and Allied Sciences, Delhi), Dwarka (Delhi), RKP (Ramakrishna
290 Puram, Delhi) in the North-West IGP; Kanpur, Lucknow in Central IGP and Patna, Muzaffarpur in
291 East IGP.

292 In addition, measurements of several aerosols, trace gases, and meteorology at Delhi (IGI
293 Airport) from the Winter Fog Experiment (WiFEX) for the period December 10-31, 2017, have also
294 been used to validate the model output. The WiFEX, an initiative of the Ministry of Earth Sciences
295 (MoES), India, is a ground-based measurement campaign at the IGI Airport Delhi to understand fog's
296 physical and chemical features. Additional details of the WiFEX project and related publications can
297 be found in Ghude et al., (2017).

298

299 **3 Meteorology Evaluation**

300 Previous studies simulating fog highlight the importance of high model vertical resolution
301 (Pithani et al., 2019; Van Der Velde et al., 2010) for representing the fog formation and the growth of
302 the fog layer, model initialization (Yadav et al., 2022), initial relative humidity (Bergot and Guedalia,
303 1994; Pithani et al., 2020), and PBL schemes (Chen et al., 2020; Pithani et al., 2019). In the present
304 study, 2-m relative humidity (RH2), 2-m temperature (T2), and 10-m wind speed (WS) from WRF-
305 Chem have been evaluated using ground-based measurements from CPCB monitoring network and
306 WIFEX campaign for nine stations across the IGP. The comparison of WRF-Chem results with
307 observations shows that RH2 and T2 are sensitive to the choice of the meteorological initial and
308 boundary conditions as illustrated by six stations in major cities (Fig. S1). WRF-Chem compares
309 better with the observations for simulations driven by the ERA-Interim reanalysis than with GFS-FNL
310 reanalysis since ERA-Interim provides more realistic RH2 than GFS-FNL (Figs. S2 a-f). For example,
311 RH2 from EXP1 (GFS) varies from 10 to 50%, while RH2 from EXP2 and EXP3 varies from 30 to
312 100%, which is closer to observation, especially for NWIGP and CIGP. For EIGP, RH2 from EXP1
313 (GFS) compares better than ERA-Interim, which overestimates the observed RH2. ERA-Interim and
314 YSU PBL scheme showed damping of RH2 continuously increasing the bias in RH2 with time (not
315 shown), which was corrected in EXP2 by refreshing meteorology every day at 00h UT during the
316 model simulation. In addition, maps of surface RH2 and T2 (Figs. S2 g-j) show that the GFS-FNL
317 dataset has lower relative humidity throughout the domain as compared to ERA-Interim. There are
318 differences in simulated 2-m temperature between these two datasets which are of smaller relative
319 magnitude compared to the RH2.

320 The GFS-FNL driven meteorology EXP1 has a warm bias in NWIGP and CIGP, especially during
321 night-time, while over EIGP, the model prediction agrees well with observations. EXP2 with the
322 ERA-Interim driven meteorology and YSU PBL scheme also shows good agreement between
323 modeled and observed T2 in EIGP. The ERA-Interim driven meteorology with the ACM2 PBL
324 scheme in EXP3 has a cold bias of up to 7°C over EIGP during daytime from 22nd to 24th December.
325 The wind speed evaluation shows that WRF-Chem is over-predicting wind speed. However, it is also
326 possible that some CPCB stations (e.g., Amritsar and RK Puram) have a wind speed low bias due to
327 the low measurement height and obstructions such as tall trees near the monitoring station as shown in
328 FigS3. WRF-chem in general overestimates wind speed and several earlier studies have reported this

329 bias in wind speed (e.g., Mohan and Gupta 2018; Pithani et al.,2019). Moreover, WRF-Chem does not
 330 have the capability to represent building meteorology and parameterizes the effects of urban areas on
 331 meteorology through roughness length, which likely leads to overestimation of wind speed. Note that
 332 at other sites (e.g., over IGI-Delhi and Kanpur) the model measurement agreement is better.

333 The WRF-Chem performance has been statistically assessed against observation using the Taylor
 334 Diagram (Taylor, 2001), which provides a statistical summary of how well the model output agrees
 335 with the observation in terms of the Pearson correlation, their centered root-mean-square error
 336 (RMSE) difference, and the ratios of their variances (Fig. 2). The centered RMS difference is
 337 proportional to the distance to point ‘‘OBS’’ in the x-axis which measures the extent to which the
 338 simulated and observed datasets match. The centered RMS difference (E'), the correlation (R), and the
 339 standard deviations, σ_m^2 (simulated) and σ_o^2 (observed) are calculated as:

$$340 \quad R = \frac{\frac{1}{N} \sum (M_n - \bar{M})(O_n - \bar{O})}{\sigma_m \sigma_o} \quad (1)$$

$$341 \quad E'^2 = \frac{1}{N} \sum [(M_n - \bar{M}) - (O_n - \bar{O})]^2 \quad (2)$$

$$342 \quad \sigma_m^2 = \frac{1}{N} \sum (M_n - \bar{M})^2 \quad (3)$$

$$343 \quad \sigma_o^2 = \frac{1}{N} \sum (O_n - \bar{O})^2 \quad (4)$$

344 where the overall mean of a field is indicated by an overbar.

345 Each point in the two-dimensional space of the Taylor diagram represents the above mentioned three
 346 different statistical metrics simultaneously, as they are related by the follow equation

$$347 \quad E'^2 = \sigma_o^2 + \sigma_m^2 - 2\sigma_o\sigma_m R \quad (5)$$

348 The diagram is constructed based on the similarity of the above equation and the Law of Cosines:

$$349 \quad c^2 = a^2 + b^2 - 2ab\cos\phi$$

350 The percentage bias has also been included to further evaluate the WRF-Chem results. In Fig.
 351 2, better agreement of WRF-Chem results with observations is shown by the marker's proximity to the
 352 ‘‘OBS’’ dashed black line. The WRF-Chem RH has a good correlation for all three experiments with r
 353 > 0.75 at all the locations in IGP for all the experiments. However, the RMSE (shown by red dashed
 354 contours) and the standard deviations are larger for EXP1 compared to EXP2 and EXP3 which lie
 355 closer to the dashed black line indicating that the simulated RH variations are similar to observations.
 356 The mean bias is also large ($>20\%$) for EXP1 (GFS-FNL) for all the stations, marked by red triangles.
 357 For example, simulated RH at Dwarka (4) and Lucknow (7) for EXP2, and IGI Airport (2), IHBAS
 358 (3), Lucknow (7), and Patna (8) for EXP3 show good agreement with observation, with $r > 0.7$,
 359 standard deviation within ± 0.25 and mean bias within 10%. Among these stations, the model performs
 360 better for Dwarka (4) and Lucknow (7) for EXP2, IGI Airport (2), and IHBAS (3) for EXP3 with a
 361 smaller centered RMSE (< 0.75).

362 For all the experiments, WRF-Chem T2 agrees well with observations with a correlation
 363 between 0.8 and 0.95. The points are concentrated near the dashed line showing a low RMSE and

364 standard deviation for T2, signifying a good agreement of simulated T2 with observation in terms of
365 temporal variation but the T2 relative bias is large for EXP1 (>20%). The RMSE and relative bias for
366 EXP1 are larger for several of the stations. For example, simulated T2 agrees best with observation at
367 IHBAS (3) for EXP1 and IGI Airport (2) for EXP2, with smaller centered RMSE and standard
368 deviation, and bias <5%. The temporal variability of T2 and RH is predicted well for all the
369 combinations of inputs (Fig. S1), however, the accuracy of simulated T2 and RH is sensitive to the
370 choice of meteorological initial/boundary conditions. WRF-Chem predicted RH and T2 agree better
371 with observations when initialized with ERA-Interim meteorology than with GFS-FNL.

372 The WRF-Chem runs driven by ERA-Interim with YSU (EXP2) and ACM2 PBL (EXP3)
373 schemes predicted the surface meteorology better over the IGP than the WRF-Chem run driven by
374 GFS (EXP1). By examining the modeled cloud water content (averaged over all the grids in the
375 analysis region) in the lowest model level with the INSAT-3D satellite fog intensity for the 23rd and
376 24th December 2017 (Fig. 3), it is apparent that WRF-Chem with the ACM2 PBL scheme compared
377 qualitatively well with observations obtained from INSAT-3D satellite in terms of fog coverage over
378 CIGP, while the WRF-Chem run with the YSU PBL scheme did not produce widespread fog.
379 However, there is also fog over EIGP in WRF-Chem with the ACM2 PBL scheme although it is not
380 observed by the satellite. This is because the model has a cold bias in T2 and a high surface RH over
381 East IGP with ACM2 PBL and Pleim-Xiu surface scheme as discussed earlier, which favors the
382 formation of fog in this region. The time series in Fig. 4 shows that EXP3 is capable of predicting the
383 duration of fog on 23rd and 24th December. There is a data gap from INSAT 3D observations because
384 it is unable to capture fog during daytime in the presence of mid and high-level clouds. Although fog
385 LWC data is available for Delhi from the WiFEx campaign, the WRF-Chem simulation does not
386 produce fog in NWIGP, therefore, the WiFEx observations are not included in this evaluation.

387 In conclusion, EXP3 is the best configuration for predicting fog formation where the ERA-
388 Interim meteorology, the ACM2 PBL and surface schemes, and soil moisture nudging is used in the
389 WRF-Chem simulation. Therefore, the evaluation of predicting AOD, surface aerosol concentrations,
390 and aerosol composition as well as analysis of the impact of aerosols on fog formation uses the EXP3
391 configuration.

392

393 **4 Aerosol Evaluation**

394 Aerosol is an important factor in correct prediction of fog (Maalick et al., 2016; Stolaki et al.,
395 2015) as the number of fog droplets depends on the aerosol size distribution and concentration.
396 Aerosols as CCN can affect the liquid water content in fog and therefore an increase in aerosol
397 concentration can significantly affect fog lifetime (Stolaki et al., 2015; Zhang et al., 2014b). AOD
398 retrievals from the MODIS satellite have been used to validate the modeled AOD (Fig. 5). It is
399 observed that the model captures several important features of the MODIS retrieved AOD spatial
400 distribution but at the same time somewhat struggles to reproduce the observed AOD magnitude in

401 some parts of the domain. One possible reason for the underestimation would be the EDGAR-HTAP
402 emission inventory, which has a low bias for residential sector PM_{2.5} emissions in India (Sharma et al.,
403 2022). For instance, the model successfully predicts high aerosol loading seen by MODIS on 20 and
404 21 December over CIGP and EIGP. This is the region with dense fog both in model and observation.
405 Higher AOD (>0.5) over CIGP and EIGP can be attributed to the accumulation of aerosols that are
406 transported by north-westerly winds to these regions from NWIGP (Dey and Di Girolamo, 2011; Jain
407 et al., 2020; Jethva et al., 2018; Kumar et al., 2018; Yadav et al., 2020). However, WRF-Chem
408 underestimates AOD over the NWIGP (AOD<0.3) throughout the simulation period and during 23-24
409 December over CIGP and EIGP where the latter may be related to enhanced scavenging of aerosols by
410 fog droplets.

411 The west to east gradient in aerosol loading over IGP is consistent with surface PM_{2.5}
412 distribution (Fig. 6a). Surface PM_{2.5} concentration is highest in EIGP (>100 µg m⁻³) and it decreases
413 gradually towards NWIGP (~60-80 µg m⁻³). The time series of PM_{2.5} from CPCB measurements and
414 the model at stations representative of each region in IGP shows that simulated PM_{2.5} compares well
415 with observation in terms of day-to-day variation over most of the locations in the IGP (Fig. 6 b-e).
416 The comparison is good over Amritsar (an NWIGP location), where PM_{2.5} is mostly primary aerosols
417 from local emissions e.g., residential heating related biomass burning. Agricultural waste burning is at
418 its peak during post monsoon months (Oct-Nov), whereas during winter burning for residential
419 heating increases and the stable boundary layer confines these emissions near the surface (Kumar et
420 al., 2021; Pawar and Sinha, 2022). PM_{2.5} at Amritsar shows a bimodal distribution with morning and
421 evening peaks whereas it is absent in the model likely due to the absence of diurnal variations in the
422 WRF-Chem anthropogenic emissions.

423 At Delhi, the daily variations are predicted well although WRF-Chem underestimates PM_{2.5}
424 observations during the first 4 days. Delhi experiences severe air pollution and haze with high PM
425 loading (> 500 µg m⁻³) (Bharali et al., 2019). The model is successful in predicting the high PM_{2.5}
426 episode on the 24th of December, but WRF-Chem underpredicts the SO₄²⁻, NH₄⁺, NO₃⁻ and Cl⁻
427 concentrations (Fig. 7). Although simulated SO₂ and NH₃ are comparable with observation, sulfate,
428 and ammonium are underestimated in the model. SO₄²⁻ is underestimated by ~ 9 µg m⁻³, while NH₄⁺,
429 NO₃⁻ and Cl⁻ are underestimated by ~30 µg m⁻³, ~19 µg m⁻³ and ~40 µg m⁻³ on average, respectively.
430 In addition, the WRF-Chem model results show that a large percentage of PM_{2.5} is classified as “other
431 inorganics”, which is usually dominated by PM_{2.5} other than BC and OC. The WiFEx observations
432 show that secondary aerosols contribute ~50% of the PM_{2.5} concentration, which is in line with other
433 studies that found secondary aerosols contribute 15-50% to PM_{2.5} mass (Sharma and Mandal, 2017;
434 Behera and Sharma, 2010; Nagar et al., 2017) and NO₃⁻ constituted 9-13% of PM_{2.5} mass (Lalchandani
435 et al., 2021; Sharma and Mandal, 2017). This leads to the underestimation of PM_{2.5} over Delhi.
436 Studies report very high chloride over the IGP with values exceeding 100 µg m⁻³ (Lalchandani et al.,
437 2021) during winter emitted from increased trash burning and industrial emissions (Pant et al., 2015;

438 Patil et al., 2013). WRF_Chem incorporates trash-burning emissions which include HCl emissions
439 from Chaudhury et al.,(2021) for this study however, the inventory contains annual emissions and fails
440 to resolve the seasonality of trash-burning emissions as identified by Nagpure et al., (2015). They
441 suggested almost all the waste-burning emissions in neighbourhoods with higher socioeconomic status
442 in Delhi occur due to the use of waste as cheap heating fuel by individuals such as night watchmen
443 and pavement dwellers. Chaudhary et al., (2021) considers waste burning that occurs due to lack of
444 collection infrastructure, and at landfills and, therefore, shows a concentration of waste burning
445 emissions around the periphery of Delhi but low waste burning emissions in the relatively prosperous
446 city centre. In addition, emissions from other sources (e.g., industries) are unaccounted for in the
447 model which likely leads to the underestimation in modeled chloride.

448 Over the CIGP and EIGP, the underestimation in PM_{2.5} is mostly observed during the dense
449 fog. It is well known that the hygroscopic aerosols grow in size and are deposited to the surface during
450 fog (Gupta and Mandariya, 2013; Kaul et al., 2011). PM_{2.5} shows an increase initially with the onset
451 of fog and then it decreases as the aerosols grow and get deposited through fog droplets. A two order
452 higher deposition rate (Fig. 6 f, g) during fog compared to the deposition rate of dry aerosol results in
453 the lower PM_{2.5} over CIGP and EICP during fog events.

454 A statistical analysis (Table S1) shows a minimum normalized mean bias (NMB) for PM_{2.5} at
455 Amritsar (2.2%), while in other stations, the normalized mean bias ranges from 48 to 53%, similar to
456 the reported range of model bias (underestimated by 40–60%) in winter over IGP by earlier studies
457 (Bran and Srivastava, 2017; Ojha et al., 2020). This was accomplished by incorporating trash-burning
458 emissions in the model simulation, which improved the PM_{2.5} prediction, increasing NMB by ~4-8%
459 in IGP. RMSE values range from 41 to 138 $\mu\text{g m}^{-3}$ (normalized RMSE~0.4 to 0.7) comparable to the
460 reported values by these studies. The Pearson correlation coefficient (r) for the simulated and observed
461 day-to-day variation in PM_{2.5} lies between 0.4 and 0.7 for all the stations in Fig. 6 except at Patna and
462 Muzaffarpur which lies within the range in these studies. The poor correlation at Patna and
463 Muzaffarpur is due to the low modeled PM_{2.5} concentrations which are caused by increased dry
464 deposition of aerosol particles activated as fog droplets during fog periods, as discussed earlier.
465 Furthermore, the fog events in WRF and observations have somewhat different time periods causing
466 WRF-predicted and the observed PM_{2.5} concentrations to decrease at different times.

467 Previous studies have reported that models tend to underestimate the AOD observation (David
468 et al., 2018; Pan et al., 2015) during the post-monsoon and winter when agricultural waste burning and
469 anthropogenic emissions dominate. While anthropogenic emissions include a contribution from the
470 residential sector, the emissions from small-scale burning for residential heating over IGP especially
471 during winter are likely underestimated in the current emission inventory (Sharma et al., 2022). This
472 leads to an underestimation of aerosol concentration in the model. Other possible causes for the
473 underestimation are the biases in the simulated meteorology (Govardhan et al., 2015; Kumar et al.,
474 2015; Pan et al., 2015) which affects the aerosol concentration. We corrected some of the biases in

475 meteorology as discussed earlier however there are still residual biases in the simulated meteorology
476 e.g., overestimation of wind speed by WRF-Chem. We also observe underestimation of secondary
477 aerosols over NWIGP which contribute significantly to the aerosol loading over IGP. Secondary
478 aerosol formation is substantial over CIGP and EIGP in the model compared to NWIGP which will be
479 discussed in a later section. The underestimation of $PM_{2.5}$ could also be linked to the uncertainty in the
480 model's chemistry scheme to simulate the secondary aerosols due to missing chemical processes or
481 due to underestimation of sulfur oxidation at different RH levels (Acharja et al., 2022; Pawar et al.,
482 2023; Ruan et al., 2022). Moreover, several modeling studies have shown significant improvements in
483 forecasting surface $PM_{2.5}$ by assimilation of satellite AOD and $PM_{2.5}$ (Ghude et al., 2020; Jena et al.,
484 2020; Kumar et al., 2020) suggesting the importance of correct initialization of the model in
485 simulating aerosols over IGP.

486

487 **5 Effect of Aerosol Radiation feedback**

488 Interactions of aerosols with radiation affects temperature and surface heat fluxes, thereby
489 weakening the turbulence in the PBL and stabilizing the boundary layer height (Fig. 8b) compared to
490 the clean environment (Fig. 8a). In the presence of well mixed aerosols within the PBL, the radiative
491 effect of aerosols lowers the noontime PBL height (Fig. 8b). However, the presence of absorbing
492 aerosols in the PBL warms the air and changes the thermodynamics. Three cases are shown in Fig.
493 8(c-e) where increases of scattering aerosol concentrations at the top of PBL (Fig. 8c) increases
494 scattering of radiation by the aerosol layer and reduces the surface reaching solar radiation similar to
495 Fig. 8b. Higher concentrations of absorbing aerosols at the top of PBL (Fig. 8d) warms the air above
496 the boundary layer and strengthens the capping inversion stabilizing the PBL and suppressing its
497 growth. The shallow PBL and weakened daytime vertical mixing confines aerosols and water vapor
498 near the surface and worsens the air quality of a region. The aerosols trapped in the stagnant PBL
499 further affects the radiation flux at the surface and creates a positive feedback loop wherein the PBL is
500 continually suppressed until interrupted by some synoptic weather phenomenon, such as the western
501 disturbances in the IGP. On the other hand, higher concentration of absorbing aerosols within the PBL
502 (Fig. 8e) warms the air in the PBL and this results in the higher PBL height. The raised PBL decreases
503 the aerosol concentration near the surface which is termed as a negative feedback effect.

504 The aerosol radiation feedback can affect shortwave heating rates (SWHR). The high aerosol
505 loading over the IGP (Fig. 6 and Fig. 7) allows the AR feedback to reduce the PBL height by more
506 than 140 m throughout the IGP compared to the surrounding region with AR feedback (Fig. 9a). The
507 difference in PBL height with and without aerosol radiation feedback is largest during noontime. The
508 suppressed PBL is due to the decrease in the surface heating flux and the consequent weakening of
509 turbulence in the PBL. The surface solar radiation flux (SWF) decreases by 5-35 % while the surface
510 latent heat (LH) and sensible heat (HFX) fluxes decrease by 5-35 % and 10-60 %, respectively (Fig.
511 S3). The stable, shallow PBL reduces the vertical mixing of aerosols and moisture and confines them

512 near the surface, resulting in increased $PM_{2.5}$ concentrations and RH near the surface with AR
513 feedback (Fig. 9). Although T2 should decrease with the reduction in surface SWF, T2 shows mixed
514 signals with both cooling and warming over IGP. While surface cooling is observed over NWIGP and
515 EIGP, T2 increases with AR feedback over most of CIGP. The response of AR feedback to T2 varies
516 in these three regions probably due to differences in the distribution and types of aerosols and the
517 presence of fog. Increase in surface concentration of $PM_{2.5}$ occurs more over NWIGP and EIGP with
518 increase in BC and OIN over NWIGP, and sulfate aerosol over EIGP which results in the surface
519 cooling due to positive AR feedback in these two regions. Over the CIGP, the AR feedback causes a
520 depletion of surface $PM_{2.5}$ (Fig. 9d), which is likely due to their hygroscopic growth, and then dry
521 deposition (average $PM_{2.5}$ dry deposition flux of $331 \mu\text{g m}^{-2} \text{hr}^{-1}$ with AR feedback and $282 \mu\text{g m}^{-2} \text{hr}^{-1}$
522 without AR feedback) in dense fog. The increase in RH with AR feedback favours the growth of
523 aerosols in size by the uptake of water

524 Examining further, the time variation of the changes in PBL height, T2, and RH between the
525 simulations with and without aerosol-radiation feedback (Fig. 9g) shows an increase in T2 while the
526 surface fluxes, sensible heat flux, latent heat flux, and downward shortwave radiation flux decrease
527 over CIGP (Fig. 9h). AR feedback affects mostly the lower atmosphere at multiple levels; however,
528 our finding suggests that the decreased shortwave radiation flux decreases the surface fluxes and thus
529 the turbulence in the boundary layer resulting in a reduced PBL height on both days. Figure 9 g and h
530 clearly show a decrease in HFX and LH following the decrease in SWF. Moreover, we observe that
531 the PBL height is sensitive to latent heat flux likely due to its strong dependence on moisture
532 availability (Xiu and Pleim, 2001; Zhang and Anthes, 1982).

533 The impact of AR feedback on T2 depends on factors such as the presence of absorbing
534 aerosols and their vertical distribution via heating or increased SWF (as observed in CIGP, Fig. S4).
535 Absorbing aerosols in WRF-Chem include BC and OIN (other inorganic aerosols), which both
536 increase near the surface (Fig. 9e, Fig. S5) due to their confinement in the stable PBL. Some areas in
537 the fog-affected region show a decrease in BC as well as SO_4^{2-} likely due to increased dry deposition
538 in fog water as discussed earlier in this section for $PM_{2.5}$. As a result, AR feedback changes the
539 absorbing to scattering ratio of aerosols over IGP indicated by the decrease in SSA (Single Scattering
540 Albedo; Fig. S6). In EIGP, sulfate concentrations are larger with AR feedback than without AR
541 feedback with time periods where the difference is $>1 \mu\text{g m}^{-3}$ (Fig.11). The BC concentration changes
542 are small ($<0.5 \mu\text{g m}^{-3}$) in the EIGP, resulting in a higher SSA near the surface with AR feedback in
543 EIGP. In the CIGP, BC concentrations increase while sulfate aerosols decrease within the PBL with
544 AR feedback (Fig.11) compared to the simulation without AR feedback. A decrease in SSA is seen for
545 the CIGP throughout the boundary layer while in EIGP the decrease occurs near the top of the PBL;
546 difference in SSA due to AR feedback is negligible in NWIGP. Also contributing to the higher SSA in
547 EIGP is the increase in RH (Fig. 9) due to AR feedback favoring the growth of aerosols in size by
548 uptake of water and the production of secondary aerosols such as SO_4^{2-} and NH_4^+ .

549 A similar observation has been made by Ramachandran et al., (2020) where SSA decreases
550 with increasing altitude due to absorbing carbonaceous aerosols at higher elevations which contributes
551 $\geq 75\%$ to the aerosol absorption over IGP. Increased shortwave heating (Fig. 10) is probably caused by
552 the increased absorbing aerosols near the surface which overwhelms the surface cooling due to
553 reduced shortwave radiation at the surface.

554 The increase in 2-m RH is substantial over CIGP on 24th December (Fig. 9g) compared to the
555 previous day following the decrease in PBL height which constrains the moisture near the surface.
556 The decrease in RH by 2% or more when aerosol-radiation feedback is included compared to no
557 aerosol-radiation feedback is likely due to increase in T2. However, the increase in RH in the
558 afternoon associated with a decrease in LH and PBL height is important for the air to saturate which
559 then favors the formation of fog in a polluted environment. Note that the increase in T2 with AR
560 feedback is very small ($< 0.5^\circ\text{C}$) which reduces further after noon ($\sim 12:30$ pm IST) on both days.

561 Another important factor that can affect the extent of change in PBL height is the distribution
562 of aerosols in the vertical (illustrated in Fig. 8). The pressure-time cross-sections of differences in T,
563 $\text{PM}_{2.5}$, BC, and SO_4^{2-} between aerosol radiation (AR) feedback (wFB) and no aerosol radiation
564 feedback (nFB) for three regions, NWIGP, CIGP, and EIGP are shown in Fig. 11. The difference in
565 the PBL height reaches a maximum with the AR feedback during midday (12:30-15:30 IST). Increase
566 in temperature in the boundary layer is observed with AR feedback particularly at the upper PBL in all
567 the regions of IGP. This induces a temperature inversion resulting in a stable and suppressed PBL. In
568 all the regions the decrease in PBL height (100-200 m) is larger on 24th December compared to 23rd
569 December. The difference in the PBL height on 23rd and 24th December with AR feedback on these
570 days is possibly controlled by the aerosol distribution during the previous day or early morning on the
571 same day. For example, in all the regions an increase in $\text{PM}_{2.5}$ is observed the previous night (23:30
572 onwards) till $\sim 11:30$ of December 24, with increased BC over NWIGP and CIGP whereas both BC
573 and SO_4^{2-} over EIGP. The increased $\text{PM}_{2.5}$ concentrations suppress the development of the PBL after
574 sunrise with AR feedback on December 24 compared to that on December 23, leading to the observed
575 differences in ΔPBL height on these two days. Increase in BC concentrations in NWIGP and CIGP are
576 found above the PBL on 24th December whereas BC concentrations decrease within the PBL. This BC
577 concentration gradient creates a temperature inversion, for example between 10:30-14:30 IST. The
578 increase in BC warms the air in the PBL; however, the warming is not strong enough to cause
579 negative feedback over CIGP. On 23rd December a small increase in BC is uniform throughout the
580 PBL, while there is a decrease in SO_4^{2-} concentrations, resulting in a warmer PBL (Fig. 11) with AR
581 feedback.

582 In EIGP, BC distribution is similar to that in CIGP with AR feedback while there is a
583 substantial increase in sulfate aerosol in the PBL. This results in the strongest extinction in EIGP as
584 evident from the largest difference in PBL height and surface cooling with AR feedback among the
585 three regions. Although ΔPBL is small on 23rd December, it still results in the accumulation of

586 aerosols during night-time (~23:30 pm onwards) which further strengthens the AR feedback effect the
587 next day in NWIGP and CIGP. Thus, AR feedback stabilizes the PBL, increases PM_{2.5} and RH in the
588 PBL making conditions favourable for persistence of fog over IGP.

589

590 **6 Effect of Aqueous phase chemistry**

591 In this section we discuss the impact of aqueous phase chemistry on aerosol composition and
592 its interaction with meteorology. There is a considerable difference in the surface concentration of
593 PM_{2.5} (>16 µg m⁻³) in the absence of aqueous chemistry over CIGP and EIGP where fog occurs (Fig.
594 12a) while the difference is negligible over NWIGP where fog does not occur. This is due to the
595 formation of secondary aerosols through aqueous phase chemistry and the hygroscopic growth of
596 aerosols during fog in these regions with the inclusion of aqueous chemistry in the model. In the
597 region between CIGP and EIGP (83E-84E; marked by the box in Fig. 12a), PM_{2.5} concentration is less
598 in the simulation with aqueous-phase chemistry than without aqueous-phase chemistry because
599 deposition of fog water aerosols to the surface increases as the fog thickens (Fig. 13, Fig. S7). Figure
600 13 shows the relation between formation of secondary aerosols, deposition flux of PM_{2.5}, and fog with
601 and without aqueous phase chemistry. During the fog event, the secondary aerosols (SO₄²⁻, NH₄⁺)
602 increase significantly by 4-10 µg m⁻³ due to aqueous phase chemistry adding to the PM_{2.5} burden over
603 IGP. The intensity of fog is high around midnight December 24-25 compared to that on 23rd and 24th
604 (1:30-11:30 IST)) which increases the dry deposition flux of PM_{2.5} causing a sharp drop in the PM_{2.5}
605 concentration on 24th December compared to the previous night's fog event. The observed change in
606 PM_{2.5} over a region is the net result of the formation of secondary aerosols and its deposition with fog
607 droplets.

608 The composition distribution of PM_{2.5} (Fig. 12b) has a similar distribution for the simulations
609 with and without aqueous phase chemistry over NWIGP where fog did not occur. The primary
610 aerosols are higher (BC > 9%, OC ~ 16-30%, OIN > 50%), than the secondary aerosols (<5%). While
611 the model requires fog for accelerated formation of secondary inorganic aerosol, experimental data
612 (Fig. 7) supports significant formation of secondary inorganic aerosol at elevated RH levels even in
613 haze aerosol (Acharja et al., 2022). On the other hand, the central and east IGP stations are fog-
614 covered and therefore, there is an increase in secondary aerosols especially SO₄²⁻ and NH₄⁺ when
615 aqueous phase chemistry is included in the simulation. SO₄²⁻ is chemically produced via aqueous
616 phase chemistry in cloud water, hence the abrupt increase whereas NH₄⁺ maintains a gas-aerosol and
617 gas-cloud equilibrium with NH₃ and SO₄²⁻ via neutralizing the drop or aerosol. NO₃⁻ is high in the
618 model compared to SO₄²⁻ and NH₄⁺ and it decreases by ~1-2 % with aqueous phase chemistry. We
619 observe a small increase in NO₃⁻ during fog, however it drops as fog intensifies, more rapidly than that
620 without aqueous phase chemistry likely due to increase in dry deposition. This results in lower
621 average NO₃⁻ to PM_{2.5} ratio with aqueous phase chemistry. Moreover, NO₃⁻ is high over the fog
622 covered CIGP and EIGP compared to NWIGP suggesting that transport and chemistry of NO_x in

623 CIGP and EIGP produce more HNO_3 . Aerosol NO_3^- is also in equilibrium with HNO_3 and it is formed
624 only if excess NH_3 is available beyond the sulfate neutralization. Thus, NH_4^+ and NO_3^- changes are
625 likely due to changing the partitioning between gas and liquid based on the production of sulfate.

626 $\text{PM}_{2.5}$ is mostly composed of organic aerosols (OA) over CIGP and EIGP (Lalchandani et al.,
627 2021; Srinivas and Sarin, 2014) whereas $\text{PM}_{2.5}$ is OIN (dust) and OA over NWIGP (Ram et al., 2012a;
628 Sharma and Mandal 2023). Although observational studies report Cl^- as one of the largest contributors
629 (12-17%) to $\text{PM}_{2.5}$ after the organics (Lalchandani et al., 2021; Pant et al., 2015) during winter, Cl^- is
630 largely underestimated by the model as discussed in section 4 and contributes only ~3%. A small
631 increase (2-4%) in secondary organic aerosols (SOA) from glyoxal production in aerosols occurs for
632 the simulation with aqueous phase chemistry included during intense fog, suggesting there are
633 feedbacks between cloud chemistry (without glyoxal aqueous chemistry) and aerosol chemistry.
634 However, similar to NO_3^- , average SOA (ASOA (anthropogenic)+BSOA (biogenic) + GlySOA)
635 shows a decrease when aqueous phase chemistry is included. SOA contributes significantly to organic
636 aerosol loading over IGP (Kaul et al., 2011; Mandariya et al., 2019).

637 The WRF-Chem results on aerosol composition during fog behave similarly to those of
638 previous observational studies. For example, Ram et al., (2012a) reported an increase of EC, OC, and
639 WSOC concentrations by ~30% during fog and haze events at Allahabad, a location in the Central
640 IGP, and a marginal increase of these constituents at Hisar (NWIGP). Several studies report an
641 increase in inorganic ions (NH_4^+ , NO_3^- , and SO_4^{2-}) during fog over IGP and elsewhere (Gundel et al.,
642 1994; Ram et al., 2012a). Recent studies suggest that a significant fraction of atmospheric particulate
643 matter in the IGP is comprised of carbonaceous aerosol (~30–35% of the PM) and water-soluble
644 inorganic species (~10–20% of the PM) during October–January when emissions from biomass
645 burning (including residential heating) are dominant over IGP (Ram et al., 2012b; Rengarajan et al.,
646 2007; Tare et al., 2006).

647 Both the simulations with and without aqueous-phase chemistry include the AR feedback. The
648 aqueous chemistry increases the mass of $\text{PM}_{2.5}$ and the size of the aerosols, both of which contribute to
649 AR feedback, thus increasing RH and PBL stability. The increase in RH also saturates the air,
650 promotes aerosol growth by water uptake, and thus favors fog formation. Since the secondary
651 inorganic aerosols are scattering aerosols, the increased scattering of radiation further reduces the
652 solar radiation reaching the surface (Fig. 14a). Over CIGP the presence of higher aerosol loading
653 reduces the T2 during daytime, particularly on the 24th of December which then reduces the PBL
654 height and increases RH near the surface (Fig. 14b). These conditions favor fog formation over the
655 CIGP. Further, the fog water content with aqueous-phase chemistry is higher than that without
656 aqueous-phase chemistry on 24th December post-midnight (Fig. 13b). This is likely due to saturation
657 of air due to increase in RH and lower T2, induced by the AR feedback caused by the increase in
658 $\text{PM}_{2.5}$. Although the difference in T2 is small (<0.4), favourable conditions mentioned above are
659 conducive to fog formation. Because aqueous chemistry increases sulfate concentrations, the size of

660 the aerosols also increase. The increased aerosol size, which can grow further by water uptake, also
661 impacts the solar radiation reaching the surface, affecting fog formation and dissipation.

662

663 **7 Effect of AR feedback and aqueous chemistry on the duration of fog**

664 Aerosol and its radiative effects impact fog characteristics, including the fog liquid water content
665 (LWC), the fog lifetime over a region and hence its spatial and temporal distribution. Variations of fog
666 LWC in WRF-Chem contrast the fog in the CIGP and EIGP (Figure 15) as well as among the three
667 experiments (with aqueous chemistry plus AR feedback, with aqueous chemistry without AR
668 feedback, and without aqueous chemistry but with AR feedback). WRF-Chem does not simulate fog
669 over NWIGP in the model for the study period. In Figure 15, only foggy grid points are considered for
670 the first fog event on 23-24 December. The LWC is 5-15% higher with AR feedback than without AR
671 feedback and without aqueous phase chemistry for both CIGP and EIGP. The interquartile range is
672 larger for the simulation with and without AR feedback than without aqueous phase chemistry in
673 CIGP showing large variability in the LWC. On the other hand, in EIGP the variability in LWC is
674 greater in the simulation with AR feedback compared to the other two experiments.

675 The formation and dissipation times of the two fog events for the three experiments are listed
676 in Tables 2 and 3 for CIGP and EIGP. The 23-24 December fog starts forming two hours earlier and
677 the 24-25 December fog forms one hour earlier in both CIGP and EIGP with AR feedback than
678 without AR feedback. In the simulation without aqueous phase chemistry, fog formation is delayed by
679 an hour or two compared to the simulation with aqueous chemistry plus AR feedback in CIGP. In
680 EIGP the 23-24 December fog forms at the same time with AR feedback and without aqueous phase
681 chemistry while the 24-25 December fog is delayed by an hour without aqueous phase chemistry. Fog
682 dissipation usually occurs after sunrise when the shortwave radiative warming at the surface warms
683 the air, which results in PBL mixing. In addition, absorbing aerosols like BC affect fog dissipation by
684 increasing the radiative heating in and above the fog. We find an increase in BC and shortwave
685 heating in the PBL with AR feedback (Fig. 10,11) and warming over CIGP with AR feedback. Fog
686 intensity starts to decrease after 01:00 UTC (06:30 IST), however, in our study, we find that the fog
687 dissipates completely in the afternoon (~10:00 UTC or 15:30 IST) for both the simulations with AR
688 feedback and no aqueous chemistry while an hour later without AR feedback in CIGP. Fog dissipation
689 is delayed in EIGP with AR feedback compared to that without AR feedback and without aqueous
690 phase chemistry. In both the regions, fog lifetime increases with AR feedback. All the stations,
691 however do not show the same pattern, for example, the 23-24 December fog in Lucknow forms and
692 dissipates at the same time for simulations with AR feedback and without aqueous phase chemistry,
693 and the 24-25 December fog forms later with AR feedback than without AR feedback. Patna shows no
694 difference in the 24-25 December fog formation in all the three experiments. To gain better insights on
695 the fog timing, we recommend that simulations at higher spatial and temporal resolutions be
696 performed to represent better the fog dynamics at point locations. Furthermore, there are other

697 important factors to consider, e.g., improved emissions, better simulations of aerosol chemical
698 composition, and evaluation of aerosol deposition.

699 The AR feedback and aqueous-phase chemistry have the potential to impact aerosol-fog
700 interactions. We can learn about the effect of the aerosol-radiation interactions on CCN concentrations
701 because the WRF-Chem model calculates the CCN concentrations at different supersaturations as a
702 diagnostic output. We compare CCN at 0.02% supersaturations, a value typical of fog, among the
703 three experiments. For the 23-24 December fog in CIGP, hourly CCN concentrations are ~10% higher
704 for the simulations with AR feedback with or without aqueous chemistry than with no AR feedback
705 (Figure S8) during the first 8 hours of the fog event (16:00-24:00 IST 23 December). Surprisingly, the
706 simulation with no aqueous chemistry has higher CCN concentrations than the simulation with
707 aqueous chemistry, as more CCN are expected with aqueous chemistry, because aqueous chemistry
708 adds sulfate to the aerosol mass increasing the mass of PM_{2.5}. Increased PM_{2.5} further contributes to
709 AR feedback, increasing RH which favours the growth of the aerosol size, categorizing more aerosols
710 as CCN. However, the dry deposition flux (ddmass) also increases in dense fog which causes rapid
711 loss in CCN and activated aerosols during fog events with the AR feedback (Fig. S7) and more so
712 without aqueous-phase chemistry. Shao et al. (2023) examined aerosol-fog interactions for two
713 consecutive fog events by comparing WRF-Chem results with current emissions strengths to those
714 with low emission strengths. They show that the first fog event promotes formation of the second fog
715 event leading to wider fog distribution, and longer fog lifetime favoured by multiple feedbacks
716 including AR feedback i.e., low temperature, high humidity and high stability similar to our study.
717 While Shao et al. (2023) observe a delay in dissipation of the first event and early formation of second
718 fog event, we find an early dissipation and early formation of fog with AR feedback as discussed
719 earlier in this section. In summary, aqueous phase chemistry together with AR feedback promotes
720 early formation of fog while AR feedback alone promotes early dissipation of fog and plays a critical
721 role in the formation and evolution of the fog over IGP.

722

723 **8 Conclusions**

724 The effects of aerosol-radiation (AR) feedback and aqueous chemistry in air quality and fog
725 have been assessed over IGP. We carried out three experiments using WRF-Chem testing different
726 combinations of PBL schemes and meteorology initial and boundary conditions. The best
727 representation of surface meteorology for the IGP region for the case study (December 20-24, 2017)
728 used ERA-Interim reanalysis to drive the meteorology and ACM2 PBL scheme with soil moisture
729 nudging to ERA-Interim. With this meteorology configuration for WRF-Chem, evaluation of aerosol
730 concentrations with measurements and the impact of aerosols on atmospheric processes during fog
731 were examined. Further, we included trash-burning emissions to represent anthropogenic chloride
732 aerosols in our configuration. Incorporation of trash burning emissions did improve the model
733 simulations of PM_{2.5} and better captured the day-to-day variability of PM_{2.5} in IGP, yet underestimated

734 its magnitude compared to CPCB observations. Moreover, secondary aerosols particularly, chloride
735 aerosols are underestimated in the model. This underestimation is likely caused by a low bias in the
736 residential burning emission inventory and a failure of the emission inventory to represent residential
737 sector emissions from the use of trash as cheap heating fuel properly. AOD regional distribution is
738 predicted well by the model for most of the IGP. However, AOD is underestimated over NWIGP
739 likely due to an underestimation of fugitive emissions during wintertime cold spells.

740 The AR interactions showed a significant impact on meteorology and air quality over IGP. A
741 WRF-chem simulation with AR interactions resulted in a lower PBL height by ~50-270 m compared
742 to a simulation without AR interactions leading to accumulation of aerosols and moisture near the
743 surface. Reduced surface shortwave radiation flux and the surface sensible and latent heat fluxes due
744 to aerosol radiative effect suppressed the turbulence resulting in a stable PBL. The shallow PBL
745 further increased surface $PM_{2.5}$ ($> 8 \mu g m^{-3}$) and RH (2-8%) over IGP and this positive feedback
746 mechanism promoted thickening of fog over IGP. However, an increase in absorbing aerosols in the
747 PBL gave negative feedback, increasing the shortwave heating and temperature particularly over
748 CIGP. Fog forms when air is saturated which occurs when the surface temperature is reduced or the
749 moisture content increases causing saturation of air. This study suggests that increase in RH saturated
750 the air and the increase in aerosols favoured fog formation as depicted by the thickening of fog
751 intensity. Aqueous phase chemistry on the other hand contributed significantly to secondary aerosols
752 in the fog, especially sulfate aerosols, indicating substantial formation of secondary aerosols in the
753 cloud. The underpredicted secondary aerosols over NWIGP where no fog occurred implies
754 underestimation of formation of aerosols through gas and aerosol chemistry in the model. This
755 underestimation could also be linked to an underestimation of pH in the default MOSAIC scheme
756 (Ruan et al., 2022) which slows the secondary aerosol formation, or an underestimation of the aqueous
757 sulfur oxidation in haze aerosol at $> 80\%$ RH before the onset of fog (Acharja et al., 2022), or missing
758 multiphase oxidation processes (Wang et al., 2022). Nevertheless, we find that the model successfully
759 simulates the same changes in the inorganic composition during fog in IGP as reported by
760 observational studies referred earlier in section 6. We also observed that AR feedback with aqueous
761 chemistry initiated the fog formation 1-2 hours earlier than the initiation time in the simulation
762 without AR feedback and without aqueous phase chemistry whereas AR feedback alone led to early
763 dissipation of fog. In addition, fog acted as an important sink of aerosols in a polluted environment
764 with increased dry deposition with cloud water. Thus, AR feedback and aqueous chemistry play a
765 significant role in modulating the distribution and concentration of aerosols and evolution of fog in the
766 PBL. Aerosol-cloud interactions were not investigated in this study due to the limitation of the ACM2
767 PBL scheme in providing necessary information with other modules in WRF. Previous studies of
768 aerosol-fog interactions have found that ACI also promotes early onset of fog formation and increases
769 fog duration (Maalick et al., 2016; Yan et al., 2021). While these previous studies were applied to

770 midlatitude fog events, it is likely that ACI also plays a dominant role in IGP fogs, suggesting that
771 future studies are needed to fully understand aerosol effects on IGP fog events.

772 The large emission of aerosols and trace gases in the IGP makes the atmospheric dynamics as
773 well as chemistry complex, suggesting the need for more studies using both models and ground-based
774 measurements to better understand the processes. While all aerosol types interact with solar radiation
775 and reduce the surface reaching flux, presence of absorbing aerosols in the boundary layer and its
776 vertical distribution plays an important role in modulating the meteorology over IGP. It is therefore
777 crucial to improve the simulation of absorbing aerosols e.g., BC in the vertical as well as at the surface
778 to increase the accuracy in predicting formation as well as the dissipation of fog in this region.
779 Emissions from burning for residential heating are an important source of aerosols in IGP during post-
780 monsoon and winter and the inclusion of these sources in the emission inventory would improve the
781 prediction of wintertime aerosols. For example, the underestimation of chloride aerosol in the model
782 indicates unaccounted emission sources over IGP and the need for more work on better quantifying
783 trash burning emissions, which may not only improve particulate chloride in the model but also
784 improve simulations of other aerosol chemical components through aerosol thermodynamics.
785 Additionally, more detailed modeling studies are required to understand the missing chemical
786 processes if any in the model which leads to biases in sulfate, nitrate and ammonium partitioning
787 between gas and aerosol phases. We find that the change in PBL height with AR feedback is sensitive
788 to changes in LH, signifying the role of soil moisture in PBL dynamics. Several studies have reported
789 cooling over IGP due to an increase in irrigation (Kumar et al., 2017; Mishra et al., 2020). Further
790 investigations into the role of irrigation in the increasing fog events over NWIGP would help in better
791 understanding the formation and persistence of fog over this region. It can be concluded that fog
792 forecasting is a complex process due to the multiple factors involved and this work suggests that AR
793 feedback is important in fog forecasting while aqueous phase chemistry plays an important role in
794 defining the composition of aerosols over IGP.

795

796 **Acknowledgement**

797 This material is based upon work supported by the NSF National Center for Atmospheric Research
798 (NCAR), which is a major facility sponsored by the U.S. National Science Foundation under
799 Cooperative Agreement No. 1852977. CB is thankful to the Fulbright Kalam Climate Fellowship
800 program under USIEF (United States – India Educational Foundation), and Women Scientist (WOS-
801 A) program, Department of Science and Technology (DST), Govt of India. The authors acknowledge
802 the use of MODIS data from NASA's Land, Atmosphere Near real-time Capability for EOS (LANCE)
803 system (<https://earthdata.nasa.gov/lance>), part of NASA's Earth Observing System Data and
804 Information System (EOSDIS); Meteorological & Oceanographic Satellite Data Archival Centre
805 (MOSDAC: <https://www.mosdac.gov.in/>), Space Applications Centre, Indian Space Research

806 Organisation, Govt. of India for INSAT-3D fog data and the Central Pollution Board of India (CPCB:
807 <https://app.cpcbcr.com/ccr/#/login>) for meteorology data. We would like to acknowledge the high-
808 performance computing support from Cheyenne (doi:10.5065/D6RX99HX) provided by NCAR's
809 Computational and Information Systems Laboratory. We thank Duseong Jo and Behrooz R, and the
810 two anonymous reviewers for their constructive comments on the manuscript.

811

812 **Data availability:** All the model simulations are archived on the NCAR campaign storage
813 (</glade/campaign/acom/acom-weather/chandrakala>) and can be accessed by contacting the
814 corresponding author. WIFEX data can be made available by contacting Dr S.D. Ghude. Trash
815 Burning emission data is available on Mendeley data (doi- <http://dx.doi.org/10.17632/t2tn4t9473.1>).
816 MODIS AOD retrievals can be downloaded from <https://earthdata.nasa.gov/>. Meteorology and
817 aerosol data from the Central Pollution Control Board (CPCB) is available at <http://cpcb.nic.in>.

818

819 **Author contributions:**

820 CB: Conceptualization, Formal Analysis, Writing

821 MB: Conceptualization, Supervision, Writing-review and editing, Funding acquisition

822 RK: Conceptualization, Supervision, Writing-review and editing

823 SDG: provided ground-based observation data, Writing-review and editing

824 VS and BS: provided trash burning emission data, Writing-review and editing

825

826 **Competing interests:** The authors declare that they have no conflict of interest.

827

828 **References**

829 Abdul-Razzak, H. and Ghan, S. J.: A parameterization of aerosol activation 3. Sectional
830 representation, *J. Geophys. Res. Atmos.*, 107(D3), AAC 1-1-AAC 1-6,
831 doi:<https://doi.org/10.1029/2001JD000483>, 2002.

832 Acharja, P., Ali, K., Ghude, S. D., Sinha, V., Sinha, B., Kulkarni, R., Gultepe, I. and Rajeevan, M. N.:
833 Enhanced secondary aerosol formation driven by excess ammonia during fog episodes in Delhi, India,
834 *Chemosphere*, 289(July 2021), 133155, doi:10.1016/j.chemosphere.2021.133155, 2022.

835 Arun, S. H., Sharma, S. K., Chaurasia, S., Vaishnav, R. and Kumar, R.: Fog/low clouds detection over
836 the delhi earth station using the ceilometer and the insat-3d/3dr satellite data, *Int. J. Remote Sens.*,
837 39(12), 4130–4144, doi:10.1080/01431161.2018.1454624, 2018.

838 Badarinath, K. V. S., Kumar Kharol, S. and Rani Sharma, A.: Long-range transport of aerosols from
839 agriculture crop residue burning in Indo-Gangetic Plains—A study using LIDAR, ground
840 measurements and satellite data, *J. Atmos. Solar-Terrestrial Phys.*, 71(1), 112–120,
841 doi:<https://doi.org/10.1016/j.jastp.2008.09.035>, 2009.

842 Banerjee, S. and Padmakumari, B.: Spatiotemporal variability and evolution of day and night winter
843 fog over the Indo Gangetic Basin using INSAT-3D and comparison with surface visibility and aerosol
844 optical depth, *Sci. Total Environ.*, 745, 140962, doi:10.1016/j.scitotenv.2020.140962, 2020.

845 Behera, S. N. and Sharma, M.: Reconstructing primary and secondary components of PM_{2.5}
846 composition for an Urban Atmosphere, *Aerosol Sci. Technol.*, 44(11), 983–992,
847 doi:10.1080/02786826.2010.504245, 2010.

848 Bergot, T. and Guedalia, D.: Numerical Forecasting of Radiation Fog. Part I: Numerical Model and
849 Sensitivity Tests, *Mon. Weather Rev.*, 122(6), 1218–1230, doi:10.1175/1520-
850 0493(1994)122<1218:NFORFP>2.0.CO;2, 1994.

851 Bharali, C., Nair, V. S., Chutia, L. and Babu, S. S.: Modeling of the Effects of Wintertime Aerosols on
852 Boundary Layer Properties Over the Indo Gangetic Plain, *J. Geophys. Res. Atmos.*, 124(7), 4141–
853 4157, doi:10.1029/2018JD029758, 2019.

854 Bodaballa, J. K., Geresdi, I., Ghude, S. D. and Salma, I.: Numerical simulation of the microphysics
855 and liquid chemical processes occur in fog using size resolving bin scheme, *Atmos. Res.*, 266,
856 105972, doi:https://doi.org/10.1016/j.atmosres.2021.105972, 2022.

857 Boutle, I., Price, J., Kudzotsa, I., Kokkola, H. and Romakkaniemi, S.: Aerosol-fog interaction and the
858 transition to well-mixed radiation fog, *Atmos. Chem. Phys.*, 18(11), 7827–7840, doi:10.5194/acp-18-
859 7827-2018, 2018.

860 Bran, S. H. and Srivastava, R.: Investigation of PM(2.5) mass concentration over India using a
861 regional climate model., *Environ. Pollut.*, 224, 484–493, doi:10.1016/j.envpol.2017.02.030, 2017.

862 Chapman, E. G., Gustafson, W. I., Easter, R. C., Barnard, J. C., Ghan, S. J., Pekour, M. S. and Fast, J.
863 D.: Coupling aerosol-cloud-radiative processes in the WRF-Chem model: Investigating the radiative
864 impact of elevated point sources, *Atmos. Chem. Phys.*, 9(3), 945–964, doi:10.5194/acp-9-945-2009,
865 2009.

866 Chaudhary, P., Garg, S., George, T., Shabin, M., Saha, S., Subodh, S. and Sinha, B.: Underreporting
867 and open burning – the two largest challenges for sustainable waste management in India, *Resour.*
868 *Conserv. Recycl.*, 175(July), 105865, doi:10.1016/j.resconrec.2021.105865, 2021.

869 Chaurasia, S. and Gohil, B. S.: Detection of Day Time Fog over India Using INSAT-3D Data, *IEEE J.*
870 *Sel. Top. Appl. Earth Obs. Remote Sens.*, 8(9), 4524–4530, doi:10.1109/JSTARS.2015.2493000,
871 2015.

872 Chaurasia, S. and Jenamani, R. K.: Detection of Fog Using Temporally Consistent, , 10(12), 5307–
873 5313, 2017.

874 Chen, C., Zhang, M., Perrie, W., Chang, R., Chen, X., Duplessis, P. and Wheeler, M.: Boundary Layer
875 Parameterizations to Simulate Fog Over Atlantic Canada Waters, *Earth Sp. Sci.*, 7(3),
876 doi:10.1029/2019EA000703, 2020.

877 David, L. M., Ravishankara, A. R., Kodros, J. K., Venkataraman, C., Sadavarte, P., Pierce, J. R.,
878 Chaliyakunnel, S. and Millet, D. B.: Aerosol Optical Depth Over India, *J. Geophys. Res. Atmos.*,
879 123(7), 3688–3703, doi:10.1002/2017JD027719, 2018.

880 Debnath, S., Karumuri, R. K., Govardhan, G., Jat, R., Saini, H., Vispute, A., Kulkarni, S. H., Jena, C.,
881 Kumar, R., Chate, D. M. and Ghude, S. D.: Implications of Implementing Promulgated and
882 Prospective Emission Regulations on Air Quality and Health in India during 2030 N3 -
883 10.4209/aaqr.220112, *AEROSOL AIR Qual. Res.* [online] Available from:
884 <http://hdl.handle.net/10754/681704>, 2022.

885 Deshpande, P., Meena, D., Tripathi, S., Bhattacharya, A. and Verma, M. K.: Event-based fog
886 climatology and typology for cities in Indo-Gangetic plains, *Urban Clim.*, 51, 101642,

887 doi:<https://doi.org/10.1016/j.uclim.2023.101642>, 2023.

888 Dey, S. and Di Girolamo, L.: A decade of change in aerosol properties over the Indian subcontinent,
889 *Geophys. Res. Lett.*, 38(14), 1–5, doi:10.1029/2011GL048153, 2011.

890 Dey, S. and Tripathi, S. N.: Estimation of aerosol optical properties and radiative effects in the Ganga
891 basin, northern India, during the wintertime, *J. Geophys. Res. Atmos.*, 112(3),
892 doi:10.1029/2006JD007267, 2007.

893 Dhangar, N. G., Lal, D. M., Ghude, S. D., Kulkarni, R., Parde, A. N., Pithani, P., Niranjana, K., Prasad,
894 D. S. V. V. D., Jena, C., Sajjan, V. S., Prabhakaran, T., Karipot, A. K., Jenamani, R. K., Singh, S. and
895 Rajeevan, M.: On the Conditions for Onset and Development of Fog Over New Delhi: An
896 Observational Study from the WiFEX, *Pure Appl. Geophys.*, 178(9), 3727–3746, doi:10.1007/s00024-
897 021-02800-4, 2021.

898 Ding, A. J., Huang, X., Nie, W., Sun, J. N., Kerminen, V. M., Petäjä, T., Su, H., Cheng, Y. F., Yang,
899 X. Q., Wang, M. H., Chi, X. G., Wang, J. P., Virkkula, A., Guo, W. D., Yuan, J., Wang, S. Y., Zhang,
900 R. J., Wu, Y. F., Song, Y., Zhu, T., Zilitinkevich, S., Kulmala, M. and Fu, C. B.: Enhanced haze
901 pollution by black carbon in megacities in China, *Geophys. Res. Lett.*, 43(6), 2873–2879,
902 doi:10.1002/2016GL067745, 2016.

903 Easter, R. C., Ghan, S. J., Zhang, Y., Saylor, R. D., Chapman, E. G., Laulainen, N. S., Abdul-Razzak,
904 H., Leung, L. R., Bian, X. and Zaveri, R. A.: MIRAGE: Model description and evaluation of aerosols
905 and trace gases, *J. Geophys. Res. D Atmos.*, 109(20), doi:10.1029/2004JD004571, 2004.

906 Emmons, L. K., Schwantes, R. H., Orlando, J. J., Tyndall, G., Kinnison, D., Lamarque, J. F., Marsh,
907 D., Mills, M. J., Tilmes, S., Bardeen, C., Buchholz, R. R., Conley, A., Gettelman, A., Garcia, R.,
908 Simpson, I., Blake, D. R., Meinardi, S. and Pétron, G.: The Chemistry Mechanism in the Community
909 Earth System Model Version 2 (CESM2), *J. Adv. Model. Earth Syst.*, 12(4), 1–21,
910 doi:10.1029/2019MS001882, 2020.

911 Emmons, L. K., Walters, S., Hess, P. G., Lamarque, J. F., Pfister, G. G., Fillmore, D., Granier, C.,
912 Guenther, A., Kinnison, D., Laepple, T., Orlando, J., Tie, X., Tyndall, G., Wiedinmyer, C.,
913 Baughcum, S. L. and Kloster, S.: Description and evaluation of the Model for Ozone and Related
914 chemical Tracers, version 4 (MOZART-4), *Geosci. Model Dev.*, 3(1), 43–67, doi:10.5194/gmd-3-43-
915 2010, 2010.

916 Fahey, K. M. and Pandis, S. N.: Optimizing model performance: variable size resolution in cloud
917 chemistry modeling, *Atmos. Environ.*, 35(26), 4471–4478, doi:[https://doi.org/10.1016/S1352-
918 2310\(01\)00224-2](https://doi.org/10.1016/S1352-2310(01)00224-2), 2001.

919 Fast, J. D., Gustafson Jr, W. I., Easter, R. C., Zaveri, R. A., Barnard, J. C., Chapman, E. G., Grell, G.
920 A. and Peckham, S. E.: Evolution of ozone, particulates, and aerosol direct forcing in an urban area
921 using a new fully-coupled meteorology, chemistry, and aerosol model, *J. Geophys. Res.*, 111(5),
922 D21305, 2006.

923 Gautam, R., Hsu, N. C., Kafatos, M. and Tsay, S.: Influences of winter haze on fog / low cloud over
924 the Indo-Gangetic plains, , 112(June 2006), 1–11, doi:10.1029/2005JD007036, 2007.

925 Ghude, S. D., Bhat, G. S., Prabhakaran, T., Jenamani, R. K., Chate, D. M., Safai, P. D., Karipot, A.
926 K., Konwar, M., Pithani, P., Sinha, V., Rao, P. S. P., Dixit, S. A., Tiwari, S., Todekar, K., Varpe, S.,
927 Srivastava, A. K., Bisht, D. S., Murugavel, P., Ali, K., Mina, U., Dharua, M., Jaya Rao, Y.,
928 Padmakumari, B., Hazra, A., Nigam, N., Shende, U., Lal, D. M., Chandra, B. P., Mishra, A. K.,
929 Kumar, A., Hakkim, H., Pawar, H., Acharja, P., Kulkarni, R., Subharthi, C., Balaji, B., Varghese, M.,

930 Bera, S. and Rajeevan, M.: Winter fog experiment over the Indo-Gangetic plains of India, *Curr. Sci.*,
931 112(4), 767–784, doi:10.18520/cs/v112/i04/767-784, 2017.

932 Ghude, S. D., Chate, D. M., Jena, C., Beig, G., Kumar, R., Barth, M. C., Pfister, G. G., Fadnavis, S.
933 and Pithani, P.: Premature mortality in India due to PM_{2.5} and ozone exposure, *Geophys. Res. Lett.*,
934 43(9), 4650–4658, doi:https://doi.org/10.1002/2016GL068949, 2016.

935 Ghude, S. D., Jenamani, R. K., Kulkarni, R., Wagh, S., Dhangar, N. G., Parde, A. N., Acharja, P.,
936 Lonkar, P., Govardhan, G., Yadav, P., Vispute, A., Debnath, S., Lal, D. M., Bisht, D. S., Jena, C.,
937 Pawar, P. V., Dhankhar, S. S., Sinha, V., Chate, D. M., Safai, P. D., Nigam, N., Konwar, M., Hazra,
938 A., Dharmaraj, T., Gopalkrishnan, V., Padmakumari, B., Gultepe, I., Biswas, M., Karipot, A. K.,
939 Prabhakaran, T., Nanjundiah, R. S. and Rajeevan, M.: WiFEX Walk into the Warm Fog over Indo-
940 Gangetic Plain Region, *Bull. Am. Meteorol. Soc.*, 104(5), E980–E1005, doi:10.1175/BAMS-D-21-
941 0197.1, 2023.

942 Ghude, S. D., Kulkarni, S. H., Jena, C., Pfister, G. G., Beig, G., Fadnavis, S. and Van Der, R. J.:
943 Application of satellite observations for identifying regions of dominant sources of nitrogen oxides
944 over the indian subcontinent, *J. Geophys. Res. Atmos.*, 118(2), 1075–1089,
945 doi:10.1029/2012JD017811, 2013.

946 Ghude, S. D., Kumar, R., Jena, C., Debnath, S., Kulkarni, R. G., Alessandrini, S., Biswas, M.,
947 Kulkrani, S., Pithani, P., Kelkar, S., Sajjan, V., Chate, D. M., Soni, V. K., Singh, S., Nanjundiah, R. S.
948 and Rajeevan, M.: Evaluation of PM_{2.5} forecast using chemical data assimilation in the WRF-Chem
949 model: A novel initiative under the Ministry of Earth Sciences Air Quality Early Warning System for
950 Delhi, India, *Curr. Sci.*, 118(11), 1803–1815, doi:10.18520/cs/v118/i11/1803-1815, 2020.

951 Govardhan, G., Nanjundiah, R. S., Satheesh, S. K., Krishnamoorthy, K. and Kotamarthi, V. R.:
952 Performance of WRF-chem over indian region: Comparison with measurements, *J. Earth Syst. Sci.*,
953 124(4), 875–896, doi:10.1007/s12040-015-0576-7, 2015.

954 Grell, G. A., Peckham, S. E., Schmitz, R., McKeen, S. A., Frost, G., Skamarock, W. C. and Eder, B.:
955 Fully coupled “online” chemistry within the WRF model, *Atmos. Environ.*, 39(37), 6957–6975,
956 doi:https://doi.org/10.1016/j.atmosenv.2005.04.027, 2005.

957 Guenther, A., Karl, T., Harley, P., Weidinmyer, C., Palmer, P. I. and Geron, C.: Edinburgh Research
958 Explorer Estimates of global terrestrial isoprene emissions using MEGAN (Model of Emissions of
959 Gases and Aerosols from Nature) and Physics Estimates of global terrestrial isoprene emissions using
960 MEGAN (Model of Emissions of Gases an, *Atmos. Chem. Phys.*, (6), 3181–3210, 2006.

961 Gundel, L. A., Benner, W. H. and Hansen, A. D. A.: Chemical composition of fog water and
962 interstitial aerosol in Berkeley, California, *Atmos. Environ.*, 28(16), 2715–2725,
963 doi:https://doi.org/10.1016/1352-2310(94)90443-X, 1994.

964 Gunwani, P. and Mohan, M.: Sensitivity of WRF model estimates to various PBL parameterizations in
965 different climatic zones over India, *Atmos. Res.*, 194(2016), 43–65,
966 doi:10.1016/j.atmosres.2017.04.026, 2017.

967 Gupta, T. and Mandariya, A.: Sources of submicron aerosol during fog-dominated wintertime at
968 Kanpur, *Environ. Sci. Pollut. Res.*, 20(8), 5615–5629, doi:10.1007/s11356-013-1580-6, 2013.

969 Hakkim, H., Sinha, V., Chandra, B. P., Kumar, A., Mishra, A. K., Sinha, B., Sharma, G., Pawar, H.,
970 Sohpaal, B., Ghude, S. D., Pithani, P., Kulkarni, R., Jenamani, R. K. and Rajeevan, M.: Volatile
971 organic compound measurements point to fog-induced biomass burning feedback to air quality in the
972 megacity of Delhi, *Sci. Total Environ.*, 689, 295–304, doi:10.1016/j.scitotenv.2019.06.438, 2019.

973 Hariprasad, K. B. R. R., Srinivas, C. V., Singh, A. B., Vijaya Bhaskara Rao, S., Baskaran, R. and
974 Venkatraman, B.: Numerical simulation and intercomparison of boundary layer structure with
975 different PBL schemes in WRF using experimental observations at a tropical site, *Atmos. Res.*, 145–
976 146, 27–44, doi:10.1016/j.atmosres.2014.03.023, 2014.

977 Hong, S. Y., Noh, Y. and Dudhia, J.: A new vertical diffusion package with an explicit treatment of
978 entrainment processes, *Mon. Weather Rev.*, 134(9), 2318–2341, doi:10.1175/MWR3199.1, 2006.

979 Jacobson, M. Z., Turco, R. P., Jensen, E. J. and Toon, O. B.: Modeling coagulation among particles of
980 different composition and size, *Atmos. Environ.*, 28(7), 1327–1338, doi:https://doi.org/10.1016/1352-
981 2310(94)90280-1, 1994.

982 Jain, S., Sharma, S. K., Vijayan, N. and Mandal, T. K.: Seasonal characteristics of aerosols (PM_{2.5}
983 and PM₁₀) and their source apportionment using PMF: A four year study over Delhi, India, Elsevier
984 Ltd., 2020.

985 Jena, C., Ghude, S. D., Kumar, R., Debnath, S., Govardhan, G., Soni, V. K., Kulkarni, S. H., Beig, G.,
986 Nanjundiah, R. S. and Rajeevan, M.: Performance of high resolution (400 m) PM_{2.5} forecast over
987 Delhi, *Sci. Rep.*, 11(1), 1–9, doi:10.1038/s41598-021-83467-8, 2021.

988 Jena, C., Ghude, S., Kulkarni, R., Debnath, S., Kumar, R., Soni, V. K., Acharja, P., Kulkarni, S.,
989 Khare, M., Kaginalkar, A., Chate, D., Ali, K., Nanjundiah, R. and Rajeevan, M.: Evaluating the
990 sensitivity of fine particulate matter (PM_{2.5}) simulations to chemical
991 mechanism in Delhi, *Atmos. Chem. Phys. Discuss.*, (3), 1–28, 2020.

992 Jenamani, R. K.: Alarming rise in fog and pollution causing a fall in maximum temperature over
993 Delhi, *Curr. Sci.*, 93(3), 314–322 [online] Available from: <http://www.jstor.org/stable/24099461>,
994 2007.

995 Jethva, H., Chand, D., Torres, O., Gupta, P., Lyapustin, A. and Patadia, F.: Agricultural burning and
996 air quality over northern india: A synergistic analysis using nasa’s a-train satellite data and ground
997 measurements, *Aerosol Air Qual. Res.*, 18(7), 1756–1773, doi:10.4209/aaqr.2017.12.0583, 2018.

998 Katata, G., Chino, M., Kobayashi, T., Terada, H., Ota, M., Nagai, H., Kajino, M., Draxler, R., Hort,
999 M. C., Malo, A., Torii, T. and Sanada, Y.: Detailed source term estimation of the atmospheric release
1000 for the Fukushima Daiichi Nuclear Power Station accident by coupling simulations of an atmospheric
1001 dispersion model with an improved deposition scheme and oceanic dispersion model, *Atmos. Chem.
1002 Phys.*, 15(2), 1029–1070, doi:10.5194/acp-15-1029-2015, 2015.

1003 Kaul, D. S., Gupta, T., Tripathi, S. N., Tare, V. and Collett, J. L.: Secondary organic aerosol: A
1004 comparison between foggy and nonfoggy days, *Environ. Sci. Technol.*, 45(17), 7307–7313,
1005 doi:10.1021/es201081d, 2011.

1006 Kedia, S., Ramachandran, S., Holben, B. N. and Tripathi, S. N.: Quantification of aerosol type, and
1007 sources of aerosols over the Indo-Gangetic Plain, *Atmos. Environ.*, 98, 607–619,
1008 doi:10.1016/j.atmosenv.2014.09.022, 2014.

1009 Knote, C., Tuccella, P., Curci, G., Emmons, L., Orlando, J. J., Madronich, S., Baró, R., Jiménez-
1010 Guerrero, P., Luecken, D., Hogrefe, C., Forkel, R., Werhahn, J., Hirtl, M., Pérez, J. L., San José, R.,
1011 Giordano, L., Brunner, D., Yahya, K. and Zhang, Y.: Influence of the choice of gas-phase mechanism
1012 on predictions of key gaseous pollutants during the AQMEII phase-2 intercomparison, *Atmos.
1013 Environ.*, 115, 553–568, doi:10.1016/j.atmosenv.2014.11.066, 2014.

1014 Krishna Moorthy, K., Suresh Babu, S., Manoj, M. R. and Satheesh, S. K.: Buildup of aerosols over the
1015 Indian Region, *Geophys. Res. Lett.*, 40(5), 1011–1014, doi:10.1002/grl.50165, 2013.

- 1016 Krishna, R. K., Panicker, A. S., Yusuf, A. M. and Ullah, B. G.: On the contribution of particulate
1017 matter (PM 2.5) to direct radiative forcing over two urban environments in India, *Aerosol Air Qual.*
1018 *Res.*, 19(2), 399–410, doi:10.4209/aaqr.2018.04.0128, 2019.
- 1019 Kulkarni, R., Jenamani, R. K., Pithani, P. and Konwar, M.: Loss to Aviation Economy Due to Winter
1020 Fog in New Delhi during the Winter of 2011 – 2016, , 1–10, 2019.
- 1021 Kulkarni, S. H., Ghude, S. D., Jena, C., Karumuri, R. K., Sinha, B., Sinha, V., Kumar, R., Soni, V. K.
1022 and Khare, M.: How Much Does Large-Scale Crop Residue Burning Affect the Air Quality in Delhi?,
1023 *Environ. Sci. Technol.*, 54(8), 4790–4799, doi:10.1021/acs.est.0c00329, 2020.
- 1024 Kumar, A. and Sarin, M. M.: Aerosol iron solubility in a semi-arid region: temporal trend and impact
1025 of anthropogenic sources, *Tellus B*, 62(2), doi:10.3402/tellusb.v62i2.16519, 2010.
- 1026 Kumar, A., Hakkim, H., Sinha, B. and Sinha, V.: Gridded 1 km × 1 km emission inventory for paddy
1027 stubble burning emissions over north-west India constrained by measured emission factors of 77
1028 VOCs and district-wise crop yield data, *Sci. Total Environ.*, 789, 148064,
1029 doi:10.1016/j.scitotenv.2021.148064, 2021.
- 1030 Kumar, M., Parmar, K. S., Kumar, D. B., Mhawish, A., Broday, D. M., Mall, R. K. and Banerjee, T.:
1031 Long-term aerosol climatology over Indo-Gangetic Plain: Trend, prediction and potential source
1032 fields, *Atmos. Environ.*, 180, 37–50, doi:10.1016/j.atmosenv.2018.02.027, 2018.
- 1033 Kumar, R., Barth, M. C., Pfister, G. G., Nair, V. S., Ghude, S. D. and Ojha, N.: What controls the
1034 seasonal cycle of black carbon aerosols in India?, *J. Geophys. Res. Atmos.*, 120(15), 7788–7812,
1035 doi:https://doi.org/10.1002/2015JD023298, 2015.
- 1036 Kumar, R., Ghude, S. D., Biswas, M., Jena, C., Alessandrini, S., Debnath, S., Kulkarni, S., Sperati, S.,
1037 Soni, V. K., Nanjundiah, R. S. and Rajeevan, M.: Enhancing Accuracy of Air Quality and
1038 Temperature Forecasts During Paddy Crop Residue Burning Season in Delhi Via Chemical Data
1039 Assimilation., 2020.
- 1040 Kumar, R., Mishra, V., Buzan, J., Kumar, R., Shindell, D. and Huber, M.: Dominant control of
1041 agriculture and irrigation on urban heat island in India, *Sci. Rep.*, 7(1), 1–11, doi:10.1038/s41598-017-
1042 14213-2, 2017.
- 1043 Lalchandani, V., Kumar, V., Tobler, A., M. Thamban, N., Mishra, S., Slowik, J. G., Bhattu, D., Rai,
1044 P., Satish, R., Ganguly, D., Tiwari, S., Rastogi, N., Tiwari, S., Močnik, G., Prévôt, A. S. H. and
1045 Tripathi, S. N.: Real-time characterization and source apportionment of fine particulate matter in the
1046 Delhi megacity area during late winter, *Sci. Total Environ.*, 770, doi:10.1016/j.scitotenv.2021.145324,
1047 2021.
- 1048 Lelieveld, J., Evans, J. S., Fnais, M., Giannadaki, D. and Pozzer, A.: The contribution of outdoor air
1049 pollution sources to premature mortality on a global scale, *Nature*, 525(7569), 367–371,
1050 doi:10.1038/nature15371, 2015.
- 1051 Ma, Y., Brooks, S. D., Vidaurre, G., Khalizov, A. F., Wang, L. and Zhang, R.: Rapid modification of
1052 cloud-nucleating ability of aerosols by biogenic emissions, *Geophys. Res. Lett.*, 40(23), 6293–6297,
1053 doi:https://doi.org/10.1002/2013GL057895, 2013.
- 1054 Maalick, Z., Kühn, T., Korhonen, H., Kokkola, H., Laaksonen, A. and Romakkaniemi, S.: Effect of
1055 aerosol concentration and absorbing aerosol on the radiation fog life cycle, *Atmos. Environ.*, 133, 26–
1056 33, doi:10.1016/j.atmosenv.2016.03.018, 2016.
- 1057 Mandariya, A. K., Gupta, T. and Tripathi, S. N.: Effect of aqueous-phase processing on the formation

1058 and evolution of organic aerosol (OA) under different stages of fog life cycles, *Atmos. Environ.*,
1059 206(November 2018), 60–71, doi:10.1016/j.atmosenv.2019.02.047, 2019.

1060 Martin, L. R. and Good, T. W.: Catalyzed oxidation of sulfur dioxide in solution: The iron-manganese
1061 synergism, *Atmos. Environ. Part A, Gen. Top.*, 25(10), 2395–2399, doi:10.1016/0960-
1062 1686(91)90113-L, 1991.

1063 Mishra, V., Ambika, A. K., Asoka, A., Aadhar, S., Buzan, J., Kumar, R. and Huber, M.: Moist heat
1064 stress extremes in India enhanced by irrigation, *Nat. Geosci.*, 13(11), 722–728, doi:10.1038/s41561-
1065 020-00650-8, 2020.

1066 Mohan, M. and Bhati, S.: Analysis of WRF Model Performance over Subtropical Region of Delhi,
1067 India, *Adv. Meteorol.*, 2011, 1–13, doi:10.1155/2011/621235, 2011.

1068 Mohan, M. and Gupta, M.: Sensitivity of PBL parameterizations on PM10 and ozone simulation using
1069 chemical transport model WRF-Chem over a sub-tropical urban airshed in India, *Atmos. Environ.*,
1070 185, 53–63, doi:10.1016/j.atmosenv.2018.04.054, 2018.

1071 Moore, R. H., Cerully, K., Bahreini, R., Brock, C. A., Middlebrook, A. M. and Nenes, A.:
1072 Hygroscopicity and composition of California CCN during summer 2010, *J. Geophys. Res. Atmos.*,
1073 117(7), 1–14, doi:10.1029/2011JD017352, 2012.

1074 Nagar, P. K., Singh, D., Sharma, M., Kumar, A., Aneja, V. P., George, M. P., Agarwal, N. and
1075 Shukla, S. P.: Characterization of PM2.5 in Delhi: role and impact of secondary aerosol, burning of
1076 biomass, and municipal solid waste and crustal matter, *Environ. Sci. Pollut. Res.*, 24(32), 25179–
1077 25189, doi:10.1007/s11356-017-0171-3, 2017.

1078 Nagpure, A. S., Ramaswami, A. and Russell, A.: Characterizing the Spatial and Temporal Patterns of
1079 Open Burning of Municipal Solid Waste (MSW) in Indian Cities, *Environ. Sci. Technol.*, 49(21),
1080 12904–12912, doi:10.1021/acs.est.5b03243, 2015.

1081 Neu, J. L. and Prather, M. J.: Toward a more physical representation of precipitation scavenging in
1082 global chemistry models: Cloud overlap and ice physics and their impact on tropospheric ozone,
1083 *Atmos. Chem. Phys.*, 12(7), 3289–3310, doi:10.5194/acp-12-3289-2012, 2012.

1084 Ojha, N., Sharma, A., Kumar, M., Girach, I., Ansari, T. U., Sharma, S. K., Singh, N., Pozzer, A. and
1085 Gunthe, S. S.: On the widespread enhancement in fine particulate matter across the Indo-Gangetic
1086 Plain towards winter, *Sci. Rep.*, 10(1), 1–9, doi:10.1038/s41598-020-62710-8, 2020.

1087 Pan, X., Chin, M., Gautam, R., Bian, H., Kim, D., Colarco, P. R., Diehl, T. L., Takemura, T., Pozzoli,
1088 L., Tsigaridis, K., Bauer, S. and Bellouin, N.: A multi-model evaluation of aerosols over South Asia:
1089 Common problems and possible causes, *Atmos. Chem. Phys.*, 15(10), 5903–5928, doi:10.5194/acp-
1090 15-5903-2015, 2015.

1091 Pant, P., Shukla, A., Kohl, S. D., Chow, J. C., Watson, J. G. and Harrison, R. M.: Characterization of
1092 ambient PM2.5 at a pollution hotspot in New Delhi, India and inference of sources, *Atmos. Environ.*,
1093 109, 178–189, doi:10.1016/j.atmosenv.2015.02.074, 2015.

1094 Patil, R. S., Kumar, R., Menon, R., Shah, M. K. and Sethi, V.: Development of particulate matter
1095 speciation profiles for major sources in six cities in India, *Atmos. Res.*, 132–133, 1–11,
1096 doi:10.1016/j.atmosres.2013.04.012, 2013.

1097 Pawar, H. and Sinha, B.: Residential heating emissions (can) exceed paddy-residue burning emissions
1098 in rural northwest India, *Atmos. Environ.*, 269, 118846,
1099 doi:https://doi.org/10.1016/j.atmosenv.2021.118846, 2022.

1100 Pawar, P. V., Ghude, S. D., Govardhan, G., Acharja, P., Kulkarni, R., Kumar, R., Sinha, B., Sinha, V.,
1101 Jena, C., Gunwani, P., Adhya, T. K., Nemitz, E. and Sutton, M. A.: Chloride (HCl / Cl⁻) dominates
1102 inorganic aerosol formation from ammonia in the Indo-Gangetic Plain during winter: modeling and
1103 comparison with observations, *Atmos. Chem. Phys.*, 23(1), 41–59, doi:10.5194/acp-23-41-2023, 2023.

1104 Pithani, P., Ghude, S. D., Chennu, V. N., Kulkarni, R. G., Steeneveld, G. J., Sharma, A., Prabhakaran,
1105 T., Chate, D. M., Gultepe, I., Jenamani, R. K. and Madhavan, R.: WRF Model Prediction of a Dense
1106 Fog Event Occurred During the Winter Fog Experiment (WIFEX), *Pure Appl. Geophys.*, 176(4),
1107 1827–1846, doi:10.1007/s00024-018-2053-0, 2019.

1108 Pithani, P., Ghude, S. D., Jenamani, R. K., Biswas, M., Naidu, C. V., Debnath, S., Kulkarni, R.,
1109 Dhangar, N. G., Jena, C., Hazra, A., Phani, R., Mukhopadhyay, P., Prabhakaran, T., Nanjundiah, R. S.
1110 and Rajeevan, M.: Real-time forecast of dense fog events over Delhi: The performance of the wrf
1111 model during the wifex field campaign, *Weather Forecast.*, 35(2), 739–756, doi:10.1175/WAF-D-19-
1112 0104.1, 2020.

1113 Pleim, J. E. and Chang, J. S.: A non-local closure model for vertical mixing in the convective
1114 boundary layer, *Atmos. Environ. Part A. Gen. Top.*, 26(6), 965–981, doi:https://doi.org/10.1016/0960-
1115 1686(92)90028-J, 1992.

1116 Pleim, J. E. and Gilliam, R.: An indirect data assimilation scheme for deep soil temperature in the
1117 Pleim-Xiu land surface model, *J. Appl. Meteorol. Climatol.*, 48(7), 1362–1376,
1118 doi:10.1175/2009JAMC2053.1, 2009.

1119 Pleim, J. E. and Xiu, A.: Development of a land surface model. Part II: Data assimilation, *J. Appl.*
1120 *Meteorol.*, 42(12), 1811–1822, doi:10.1175/1520-0450(2003)042<1811:DOALSM>2.0.CO;2, 2003.

1121 Pleim, J. E.: A combined local and nonlocal closure model for the atmospheric boundary layer. Part I:
1122 Model description and testing, *J. Appl. Meteorol. Climatol.*, 46(9), 1383–1395,
1123 doi:10.1175/JAM2539.1, 2007a.

1124 Pleim, J. E.: A combined local and nonlocal closure model for the atmospheric boundary layer. Part II:
1125 Application and evaluation in a mesoscale meteorological model, *J. Appl. Meteorol. Climatol.*, 46(9),
1126 1396–1409, doi:10.1175/JAM2534.1, 2007b.

1127 Powers, J. G., Klemp, J. B., Skamarock, W. C., Davis, C. A., Dudhia, J., Gill, D. O., Coen, J. L.,
1128 Gochis, D. J., Ahmadov, R., Peckham, S. E., Grell, G. A., Michalakes, J., Trahan, S., Benjamin, S. G.,
1129 Alexander, C. R., Dimego, G. J., Wang, W., Schwartz, C. S., Romine, G. S., Liu, Z., Snyder, C.,
1130 Chen, F., Barlage, M. J., Yu, W. and Duda, M. G.: The weather research and forecasting model:
1131 Overview, system efforts, and future directions, *Bull. Am. Meteorol. Soc.*, 98(8), 1717–1737,
1132 doi:10.1175/BAMS-D-15-00308.1, 2017.

1133 Pye, H. O. T., Nenes, A., Alexander, B., Ault, A. P., Barth, M. C., Clegg, S. L., Collett, J. L., Fahey,
1134 K. M., Hennigan, C. J., Herrmann, H., Kanakidou, M., Kelly, J. T., Ku, I. T., Faye McNeill, V.,
1135 Riemer, N., Schaefer, T., Shi, G., Tilgner, A., Walker, J. T., Wang, T., Weber, R., Xing, J., Zaveri, R.
1136 A. and Zuend, A.: The acidity of atmospheric particles and clouds., 2020.

1137 Ram, K., Sarin, M. M. and Tripathi, S. N.: Temporal trends in atmospheric PM 2.5, PM 10, elemental
1138 carbon, organic carbon, water-soluble organic carbon, and optical properties: Impact of biomass
1139 burning emissions in the Indo-Gangetic Plain, *Environ. Sci. Technol.*, 46(2), 686–695,
1140 doi:10.1021/es202857w, 2012b.

1141 Ram, K., Sarin, M. M., Sudheer, A. K. and Rengarajan, R.: Carbonaceous and secondary inorganic
1142 aerosols during wintertime fog and haze over urban sites in the Indo-Gangetic plain, *Aerosol Air Qual.*

- 1143 Res., 12(3), 355–366, doi:10.4209/aaqr.2011.07.0105, 2012a.
- 1144 Ramachandran, S., Rupakheti, M. and Lawrence, M. G.: Aerosol-induced atmospheric heating rate
1145 decreases over South and East Asia as a result of changing content and composition, *Sci. Rep.*, 10(1),
1146 1–17, doi:10.1038/s41598-020-76936-z, 2020.
- 1147 Rengarajan, R., Sarin, M. M. and Sudheer, A. K.: Carbonaceous and inorganic species in atmospheric
1148 aerosols during wintertime over urban and high-altitude sites in North India, *J. Geophys. Res. Atmos.*,
1149 112(21), 1–16, doi:10.1029/2006JD008150, 2007.
- 1150 Ruan, X., Zhao, C., Zaveri, R. A., He, P., Wang, X., Shao, J. and Geng, L.: Simulations of aerosol pH
1151 in China using WRF-Chem (v4 . 0): sensitivities of aerosol pH and its temporal variations during
1152 haze episodes, , 6143–6164, 2022.
- 1153 Safai, P. D., Ghude, S., Pithani, P., Varpe, S., Kulkarni, R., Todekar, K., Tiwari, S., Chate, D. M.,
1154 Prabhakaran, T., Jenamani, R. K. and Rajeevan, M. N.: Two-way relationship between aerosols and
1155 fog: A case study at IGI airport, New Delhi, *Aerosol Air Qual. Res.*, 19(1), 71–79,
1156 doi:10.4209/aaqr.2017.11.0542, 2019.
- 1157 Sarkar, C., Roy, A., Chatterjee, A., Ghosh, S. K. and Raha, S.: Factors controlling the long-term
1158 (2009–2015) trend of PM_{2.5} and black carbon aerosols at eastern Himalaya, India, *Sci. Total*
1159 *Environ.*, 656, 280–296, doi:10.1016/j.scitotenv.2018.11.367, 2019.
- 1160 Sarkar, S., Chokngamwong, R., Cervone, G., Singh, R. P. and Kafatos, M.: Variability of aerosol
1161 optical depth and aerosol forcing over India, *Adv. Sp. Res.*, 37(12), 2153–2159,
1162 doi:10.1016/j.asr.2005.09.043, 2006.
- 1163 Sengupta, A., Govardhan, G., Debnath, S., Yadav, P., Kulkarni, S. H., Parde, A. N., Lonkar, P.,
1164 Dhangar, N., Gunwani, P., Wagh, S., Nivdange, S., Jena, C., Kumar, R. and Ghude, S. D.: Probing
1165 into the wintertime meteorology and particulate matter (PM_{2.5} and PM₁₀) forecast over Delhi,
1166 *Atmos. Pollut. Res.*, 13(6), 101426, doi:https://doi.org/10.1016/j.apr.2022.101426, 2022.
- 1167 Shao, N., Lu, C., Jia, X., Wang, Y., Li, Y., Yin, Y., Zhu, B., Zhao, T., Liu, D., Niu, S., Fan, S., Yan,
1168 S. and Lv, J.: Self-enhanced aerosol – fog interactions in two successive radiation fog events in the
1169 Yangtze River Delta , China : A simulation study, , (January), 1–46, 2023.
- 1170 Sharma, A. R., Kharol, S. K., Badarinath, K. V. S. and Singh, D.: Impact of agriculture crop residue
1171 burning on atmospheric aerosol loading - A study over Punjab State, India, *Ann. Geophys.*, 28(2),
1172 367–379, doi:10.5194/angeo-28-367-2010, 2010.
- 1173 Sharma, G., Annadate, S. and Sinha, B.: Will open waste burning become India ’ s largest air
1174 pollution source ? ☆, *Environ. Pollut.*, 292(PA), 118310, doi:10.1016/j.envpol.2021.118310, 2022.
- 1175 Sharma, S. K. and Mandal, T. K.: Chemical composition of fine mode particulate matter (PM_{2.5}) in
1176 an urban area of Delhi, India and its source apportionment, *Urban Clim.*, 21, 106–122,
1177 doi:10.1016/j.uclim.2017.05.009, 2017.
- 1178 Sharma, S. K. and Mandal, T. K.: Elemental Composition and Sources of Fine Particulate Matter
1179 (PM_{2.5}) in Delhi, India, *Bull. Environ. Contam. Toxicol.*, 110(3), 1–8, doi:10.1007/s00128-023-
1180 03707-7, 2023.
- 1181 Shin, H. H. and Hong, S. Y.: Intercomparison of Planetary Boundary-Layer Parametrizations in the
1182 WRF Model for a Single Day from CASES-99, *Boundary-Layer Meteorol.*, 139(2), 261–281,
1183 doi:10.1007/s10546-010-9583-z, 2011.
- 1184 Singh, A. and Dey, S.: Influence of aerosol composition on visibility in megacity Delhi, *Atmos.*

1185 Environ., 62, 367–373, doi:10.1016/j.atmosenv.2012.08.048, 2012.

1186 Singh, N., Banerjee, T., Raju, M. P., Deboudt, K., Sorek-Hamer, M., Singh, R. S. and Mall, R. K.:
 1187 Aerosol chemistry, transport, and climatic implications during extreme biomass burning emissions
 1188 over the Indo-Gangetic Plain, Atmos. Chem. Phys., 18(19), 14197–14215, doi:10.5194/acp-18-14197-
 1189 2018, 2018.

1190 Srinivas, B. and Sarin, M. M.: PM_{2.5}, EC and OC in atmospheric outflow from the Indo-Gangetic
 1191 Plain: Temporal variability and aerosol organic carbon-to-organic mass conversion factor, Sci. Total
 1192 Environ., 487(1), 196–205, doi:10.1016/j.scitotenv.2014.04.002, 2014.

1193 Srivastava, P., Dey, S., Srivastava, A. K., Singh, S. and Tiwari, S.: Most probable mixing state of
 1194 aerosols in Delhi NCR, northern India, Atmos. Res., 200(September 2017), 88–96,
 1195 doi:10.1016/j.atmosres.2017.09.018, 2018.

1196 Steeneveld, G. J., Ronda, R. J. and Holtslag, A. A. M.: The Challenge of Forecasting the Onset and
 1197 Development of Radiation Fog Using Mesoscale Atmospheric Models, Boundary-Layer Meteorol.,
 1198 154(2), 265–289, doi:10.1007/s10546-014-9973-8, 2015.

1199 Stolaki, S., Haeffelin, M., Lac, C., Dupont, J. C., Elias, T. and Masson, V.: Influence of aerosols on
 1200 the life cycle of a radiation fog event. A numerical and observational study, Atmos. Res., 151, 146–
 1201 161, doi:10.1016/j.atmosres.2014.04.013, 2015.

1202 Syed, F. S., Körnich, H. and Tjernström, M.: On the fog variability over south Asia, Clim. Dyn.,
 1203 39(12), 2993–3005, doi:10.1007/s00382-012-1414-0, 2012.

1204 Tare, V., Tripathi, S. N., Chinnam, N., Srivastava, A. K., Dey, S., Manar, M., Kanawade, V. P.,
 1205 Agarwal, A., Kishore, S., Lal, R. B. and Sharma, M.: Measurements of atmospheric parameters during
 1206 Indian Space Research Organization Geosphere Biosphere Program Land Campaign II at a typical
 1207 location in the Ganga basin: 2. Chemical properties, J. Geophys. Res. Atmos., 111(23),
 1208 doi:10.1029/2006JD007279, 2006.

1209 Tav, J., Masson, O., Burnet, F., Paulat, P., Bourriane, T., Conil, S. and Pourcelot, L.: Determination
 1210 of fog-droplet deposition velocity from a simple weighing method, Aerosol Air Qual. Res., 18(1),
 1211 103–113, doi:10.4209/aaqr.2016.11.0519, 2018.

1212 Taylor, K. E.: in a Single Diagram, , 106, 7183–7192, 2001.

1213 Van Der Velde, I. R., Steeneveld, G. J., Wichers Schreur, B. G. J. and Holtslag, A. A. M.: Modeling
 1214 and forecasting the onset and duration of severe radiation fog under frost conditions, Mon. Weather
 1215 Rev., 138(11), 4237–4253, doi:10.1175/2010MWR3427.1, 2010.

1216 Verma, S., Ramana, M. V. and Kumar, R.: Atmospheric rivers fueling the intensification of fog and
 1217 haze over Indo-Gangetic Plains, Sci. Rep., 12(1), 1–9, doi:10.1038/s41598-022-09206-9, 2022.

1218 Wang, T., Liu, M., Liu, M., Song, Y., Xu, Z., Shang, F., Huang, X., Liao, W., Wang, W., Ge, M., Cao,
 1219 J., Hu, J., Tang, G., Pan, Y., Hu, M. and Zhu, T.: Sulfate Formation Apportionment during Winter
 1220 Haze Events in North China, Environ. Sci. Technol., 56(12), 7771–7778, doi:10.1021/acs.est.2c02533,
 1221 2022.

1222 Wexler, A. S., Lurmann, F. W. and Seinfeld, J. H.: Modelling urban and regional aerosols—I. model
 1223 development, Atmos. Environ., 28(3), 531–546, doi:https://doi.org/10.1016/1352-2310(94)90129-5,
 1224 1994.

1225 Wiedinmyer, C., Akagi, S. K., Yokelson, R. J., Emmons, L. K., Al-Saadi, J. A., Orlando, J. J. and
 1226 Soja, A. J.: The Fire INventory from NCAR (FINN): A high resolution global model to estimate the

1227 emissions from open burning, *Geosci. Model Dev.*, 4(3), 625–641, doi:10.5194/gmd-4-625-2011,
1228 2011.

1229 Xie, B., Fung, J. C. H., Chan, A. and Lau, A.: Evaluation of nonlocal and local planetary boundary
1230 layer schemes in the WRF model, *J. Geophys. Res. Atmos.*, 117(12), 1–26,
1231 doi:10.1029/2011JD017080, 2012.

1232 Xiu, A. and Pleim, J. E.: Development of a land surface model. Part I: Application in a mesoscale
1233 meteorological model, *J. Appl. Meteorol.*, 40(2), 192–209, doi:10.1175/1520-
1234 0450(2001)040<0192:DOALSM>2.0.CO;2, 2001.

1235 Yadav, P., Parde, A. N., Dhangar, N. G., Govardhan, G., Lal, D. M., Wagh, S., Prasad, D. S. V. V. D.,
1236 Ahmed, R. and Ghude, S. D.: Understanding the genesis of a dense fog event over Delhi using
1237 observations and high-resolution model experiments, *Model. Earth Syst. Environ.*,
1238 doi:10.1007/s40808-022-01463-x, 2022.

1239 Yadav, R., Bhatti, M. S., Kansal, S. K., Das, L., Gilhotra, V., Sugha, A., Hingmire, D., Yadav, S.,
1240 Tandon, A., Bhatti, R., Goel, A. and Mandal, T. K.: Comparison of ambient air pollution levels of
1241 Amritsar during foggy conditions with that of five major north Indian cities: multivariate analysis and
1242 air mass back trajectories, *SN Appl. Sci.*, 2(11), 1–11, doi:10.1007/s42452-020-03569-2, 2020.

1243 Yan, S., Zhu, B., Zhu, T., Shi, C. and Liu, D.: The Effect of Aerosols on Fog Lifetime : Observational
1244 Evidence and Model Simulations *Geophysical Research Letters*, , 1–10, doi:10.1029/2020GL091156,
1245 2021.

1246 Yu, H., Liu, S. C. and Dickinson, R. E.: Radiative effects of aerosols on the evolution of the
1247 atmospheric boundary layer, *J. Geophys. Res. Atmos.*, 107(12), doi:10.1029/2001jd000754, 2002.

1248 Zaveri, R. A., Easter, R. C. and Peters, L. K.: A computationally efficient Multicomponent
1249 Equilibrium Solver for Aerosols (MESA), *J. Geophys. Res. Atmos.*, 110(24), 1–22,
1250 doi:10.1029/2004JD005618, 2005.

1251 Zaveri, R. A., Easter, R. C., Fast, J. D. and Peters, L. K.: Model for Simulating Aerosol Interactions
1252 and Chemistry (MOSAIC), *J. Geophys. Res. Atmos.*, 113(13), 1–29, doi:10.1029/2007JD008782,
1253 2008.

1254 Zhang, D. and Anthes, R. A.: A High-Resolution Model of the Planetary Boundary Layer—Sensitivity
1255 Tests and Comparisons with SESAME-79 Data, *J. Appl. Meteorol. Climatol.*, 21(11), 1594–1609,
1256 doi:10.1175/1520-0450(1982)021<1594:AHRMOT>2.0.CO;2, 1982.

1257 Zhang, F., Li, Y., Li, Z., Sun, L., Li, R., Zhao, C., Wang, P., Sun, Y., Liu, X., Li, J., Li, P., Ren, G.
1258 and Fan, T.: Aerosol hygroscopicity and cloud condensation nuclei activity during the AC3Exp
1259 campaign: Implications for cloud condensation nuclei parameterization, *Atmos. Chem. Phys.*, 14(24),
1260 13423–13437, doi:10.5194/acp-14-13423-2014, 2014a.

1261 Zhang, X., Musson-Genon, L., Dupont, E., Milliez, M. and Carissimo, B.: On the Influence of a
1262 Simple Microphysics Parametrization on Radiation Fog Modelling: A Case Study During ParisFog,
1263 *Boundary-Layer Meteorol.*, 151(2), 293–315, doi:10.1007/s10546-013-9894-y, 2014b.

1264

1265

1266

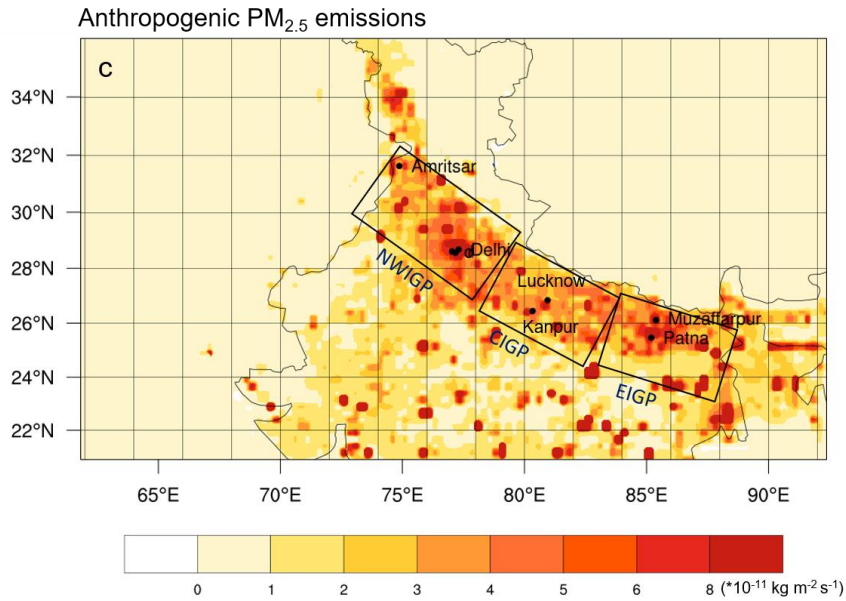
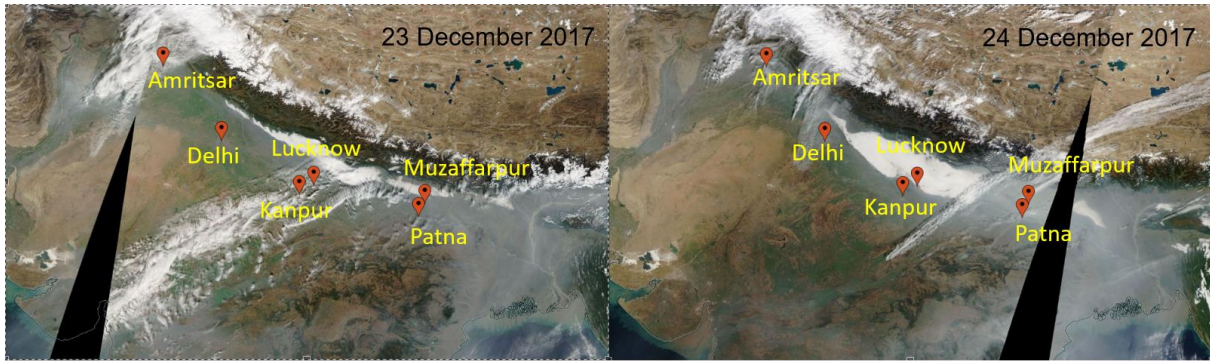
1267

1268
 1269
 1270
 1271
 1272

Table 1 Experiment set-up for the study. Numbers in parentheses for the physics options denote the namelist settings of the WRF-Chem model.

	EXP 1	EXP 2	EXP 3
Meteorology Initial /lateral boundary Condition:	<i>NCEP Final Analysis (GFS-FNL), 1° x 1°, 6 hourly</i>	<i>ERA-Interim Project, 1.125° x 0.703°, 6 hourly</i>	<i>ERA-Interim Project, 1.125° x 0.703°, 6 hourly</i>
Physics Options			
Cloud Physics	<i>Morrison 2-mom (10)</i>	<i>Morrison 2- mom (10)</i>	<i>Morrison 2- mom (10)</i>
Longwave Radiation	<i>RRTMG scheme (4)</i>	<i>RRTMG scheme (4)</i>	<i>RRTMG scheme (4)</i>
Shortwave Radiation	<i>Goddard shortwave (2)</i>	<i>RRTMG scheme (4)</i>	<i>RRTMG scheme (4)</i>
Surface Layer Physics	<i>Revised MM5 Monin-Obukhov scheme (1)</i>	<i>Revised MM5 Monin-Obukhov scheme (1)</i>	<i>Pleim-Xiu (7)</i>
Surface Model	<i>unified Noah land-surface model (2)</i>	<i>NoahMP (4)</i>	<i>Pleim-Xiu (7)</i>
PBL Scheme	<i>YSU scheme (1)</i>	<i>YSU (1)</i>	<i>ACM2 (7)</i>
Convective Parameterization	<i>Grell-Freitas (3)</i>	<i>Grell-Freitas (3)</i>	<i>Grell-Freitas (3)</i>
	<i>Continuous simulation</i>	<i>*Meteorology refreshed every 24 hr</i>	<i>**Continuous simulation: Soil nudging included</i>

1273
 1274
 1275

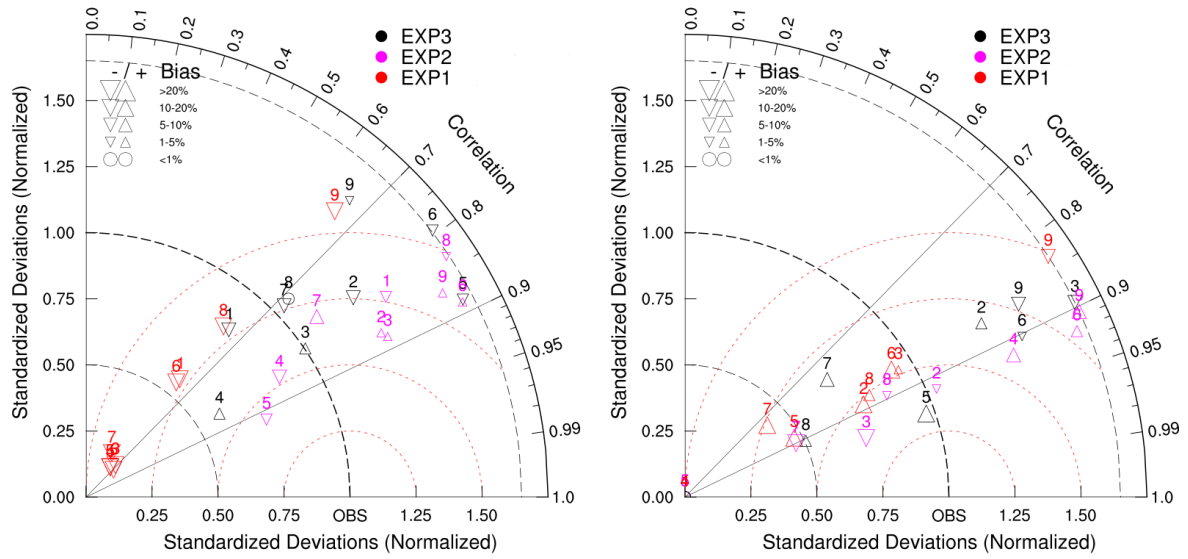


1276

1277 Figure 1 The MODIS reflectance (true color) map representing low cloud over Indo Gangetic Plains,
 1278 India (study region) indicative of likely fog and haze on 23rd December (a) and 24th December (b)
 1279 2017. (c) Anthropogenic emission of PM_{2.5} over IGP for December 2017 obtained from EDGAR-
 1280 HTAP. The boxes represent the regions Northwest IGP (NWIGP), Central IGP (CIGP), and East IGP
 1281 (EIGP).

1282

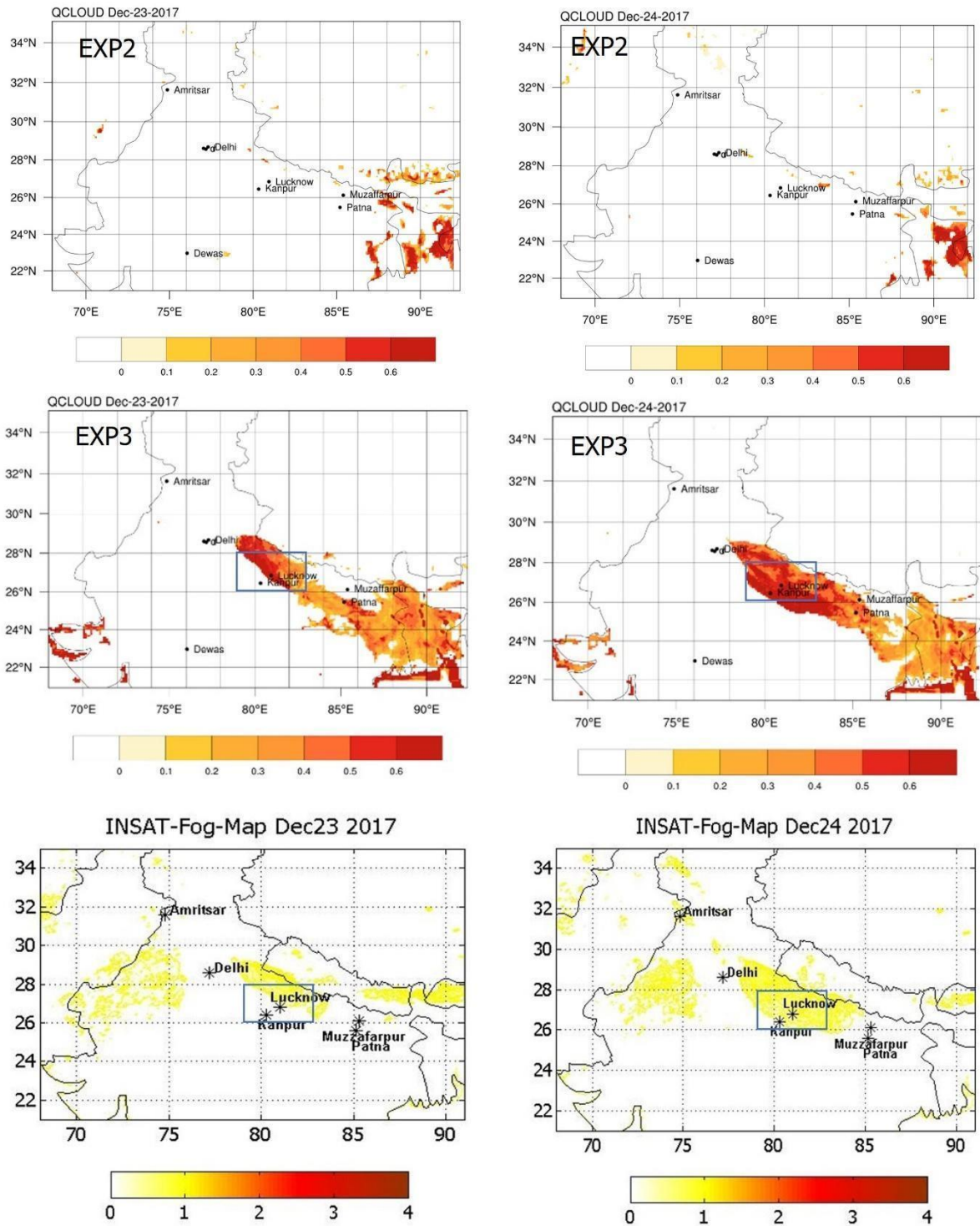
1283



1284

1285 Figure 2 Taylor Diagram of simulated (WRF-Chem) and observed (CPCB) relative humidity (left) and
 1286 2-m temperature (right) over IGP. The colors indicate the experiments. The red dotted contours
 1287 represent RMS values. The marker (triangles) size varies with a mean bias between the experiments
 1288 and observation. Upside-down triangles represent positive bias (exp-obs) and vice versa. The stations
 1289 over IGP are denoted by number 1. Amritsar, 2. IGI Airport (Delhi), 3. IHBAS (Delhi), 4. Dwarka
 1290 (Delhi), 5. RKP (Delhi), 6. Kanpur, 7. Lucknow, 8. Patna, 9. Muzaffarpur. The locations are marked
 1291 in Fig.1a.

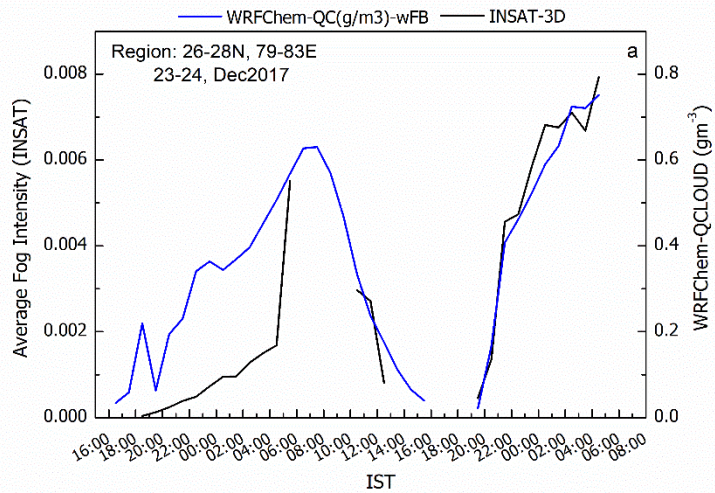
1292



1293

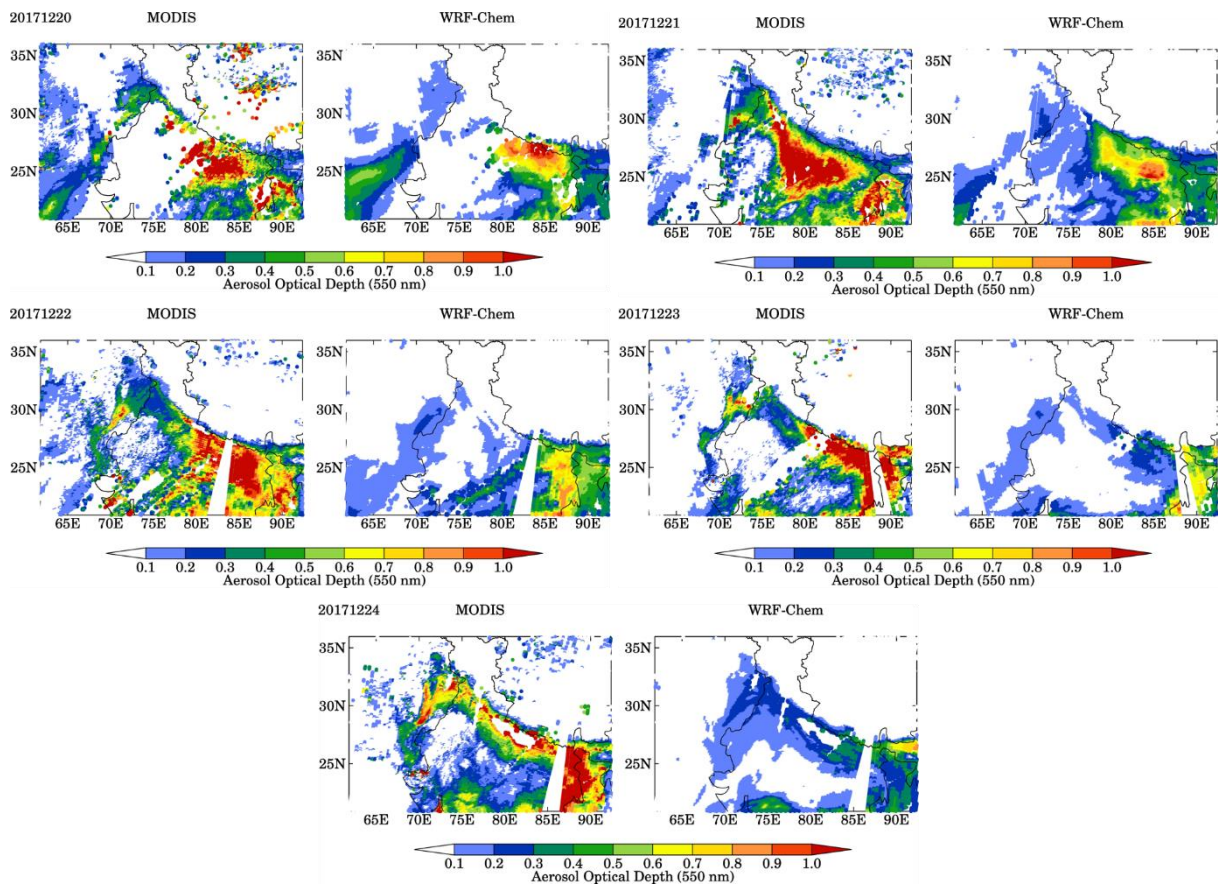
1294 Figure 3 Average WRF-Chem surface layer cloud water mixing ratios (g m^{-3}) for EXP2 and EXP3
 1295 (top four panels) and INSAT-3D satellite fog intensity (bottom two panels) on 23 and 24 December
 1296 2017. INSAT-3D satellite fog intensity varies from 0 to 4 indicating SHALLOW, MODERATE,
 1297 DENSE, and VERY_DENSE, respectively. The rectangle in central IGP is the region for the time
 1298 series analysis.

1299



1300
1301
1302
1303
1304
1305

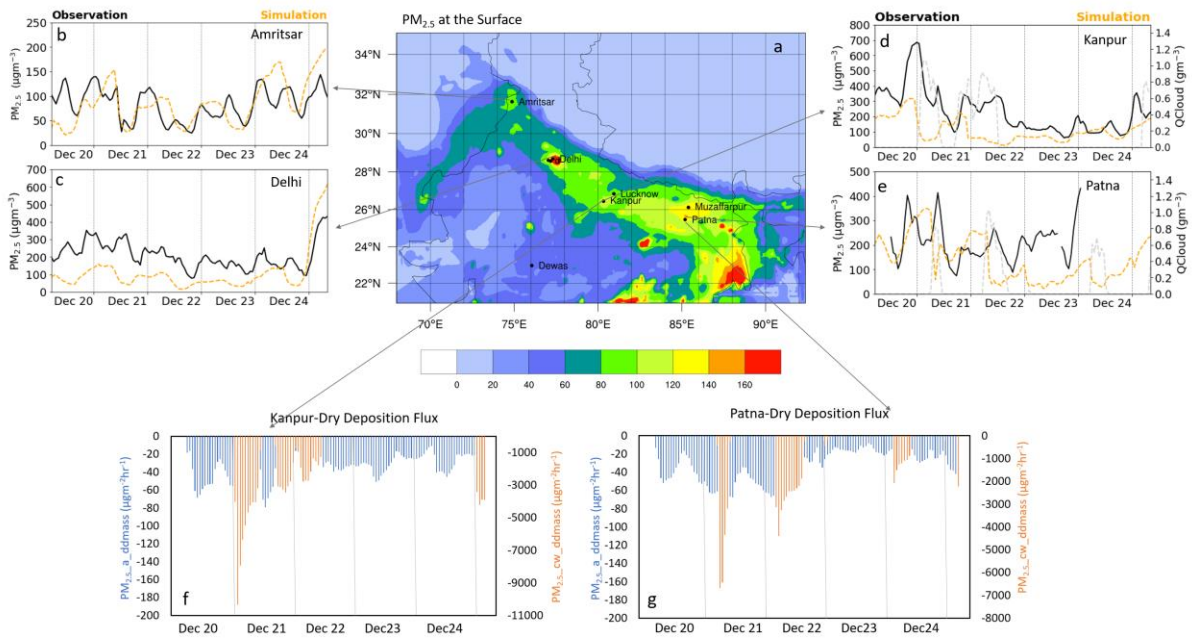
Figure 4 Average Hourly variation of fog on 23 and 24 December 2017 from WRF-Chem EXP3 simulation and INSAT-3D satellite between 26°N-28°N,79°E-83°E (region shown in Fig 3). The time is in IST (Indian Standard Time; IST is 5.5 hours ahead of Universal Time Coordinate (UTC)).



1306
1307
1308
1309
1310

Figure 5 Comparison of WRF-Chem AOD with MODIS observation over the model domain on 20, 21, 22, 23, and 24 December 2017.

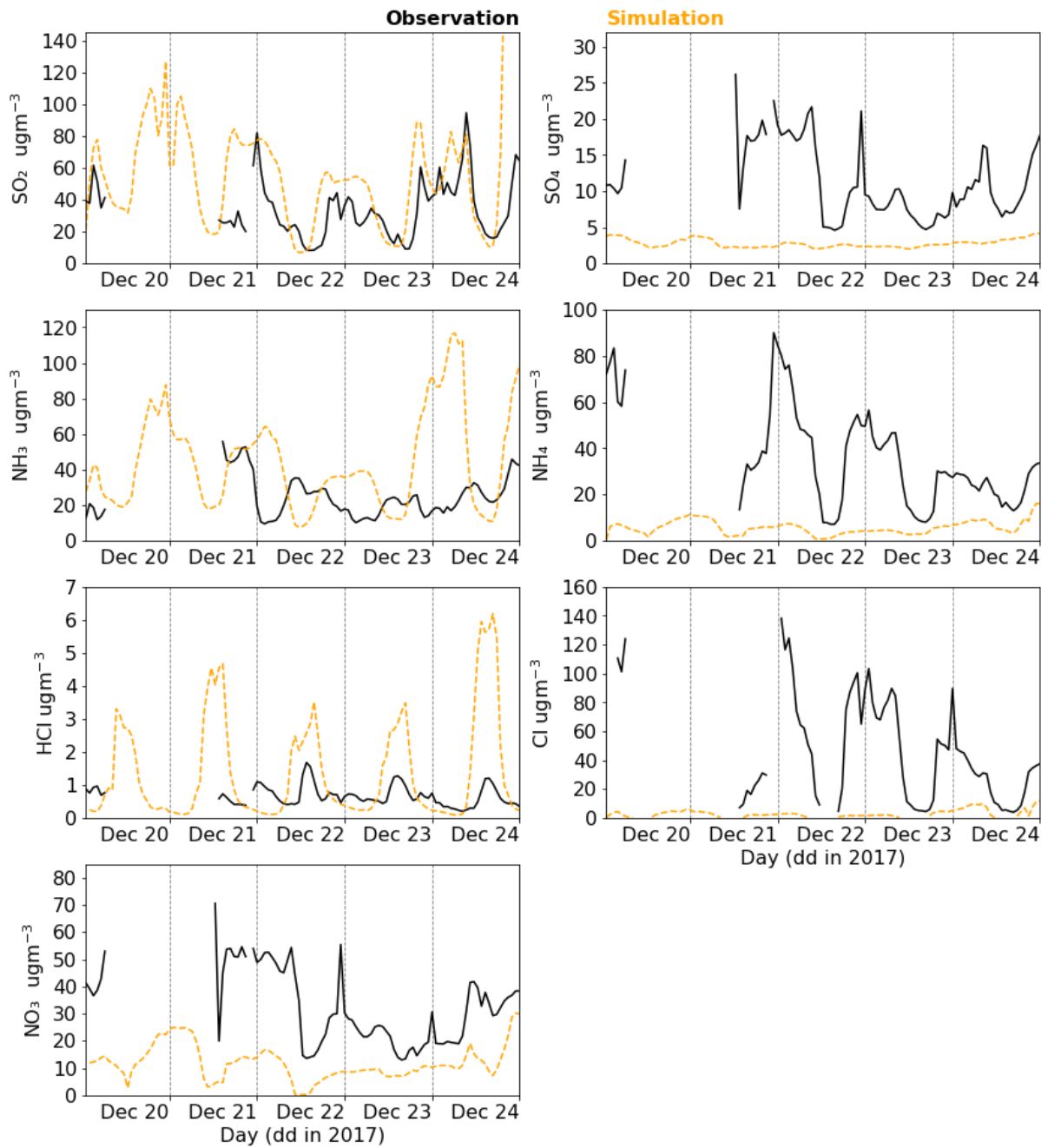
1311



1312

1313 Figure 6 WRF-Chem simulated surface PM_{2.5} map over IGP (a); comparison of WRF-Chem PM_{2.5}
1314 with CPCB observation for the period 20-24 Dec 2017 for (b) Amritsar, (c) Delhi, (d) Kanpur and (e)
1315 Patna. Dry Deposition rate of PM_{2.5} for (f) Kanpur and (g) Patna. The grey dotted line in (d) Kanpur
1316 and (e) Patna is fog (QCloud) present during the study period.

1317

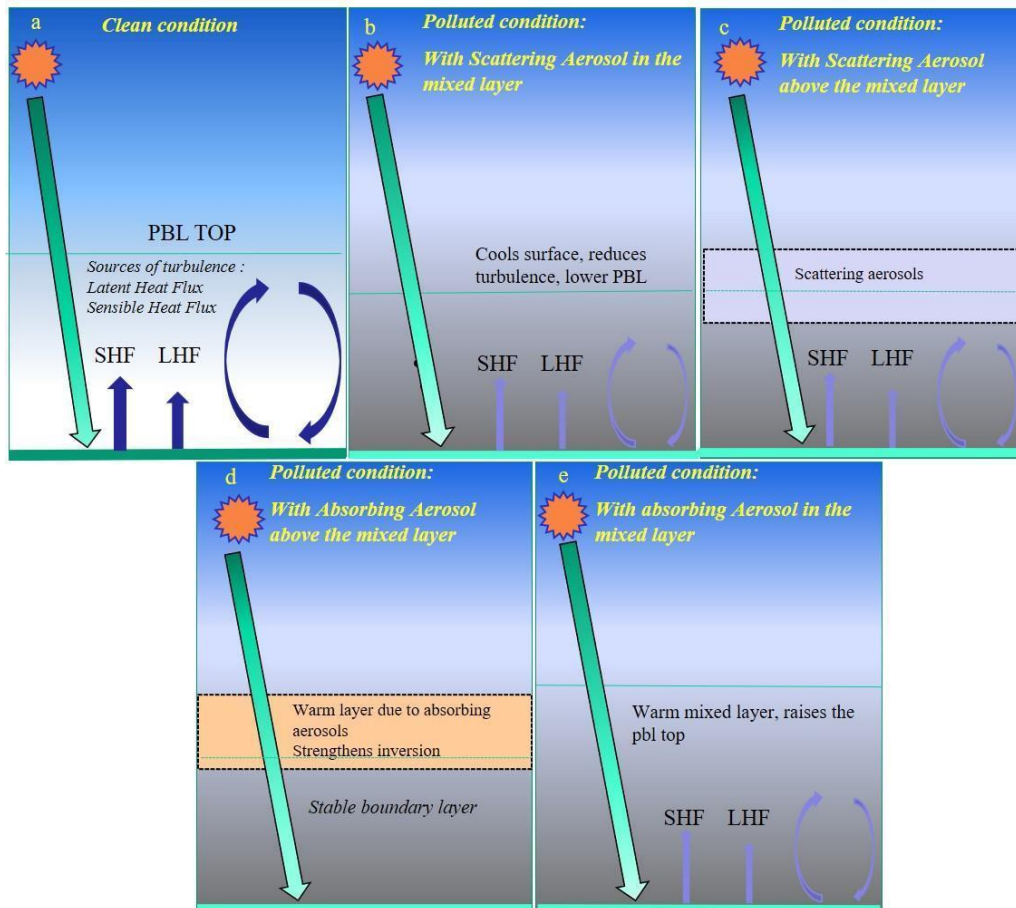


1318
 1319 Figure 7 Comparison of WRF-Chem simulated ions (SO_4^{2-} , NH_4^+ , NO_3^- , Cl^-) and trace gases (SO_2 ,
 1320 NH_3 & HCl) with the observation from WIFEX campaign at Delhi.

1321

1322

1323

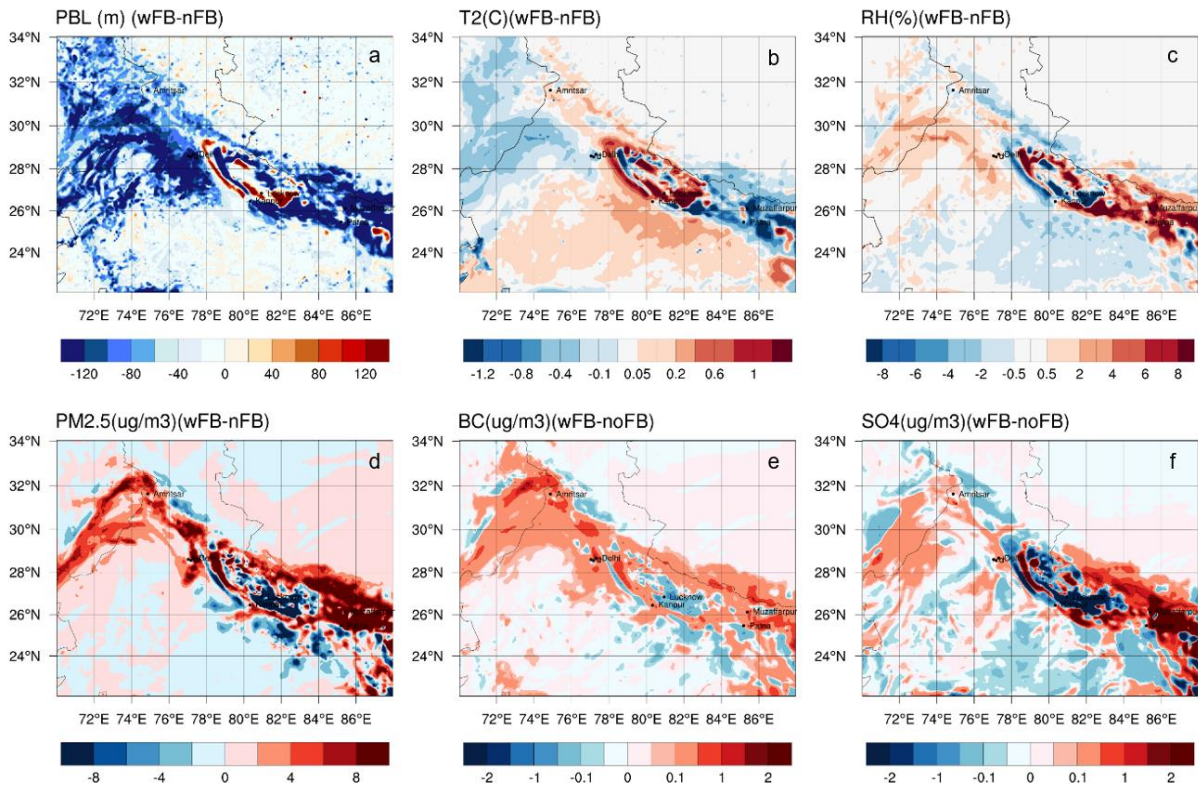


1324

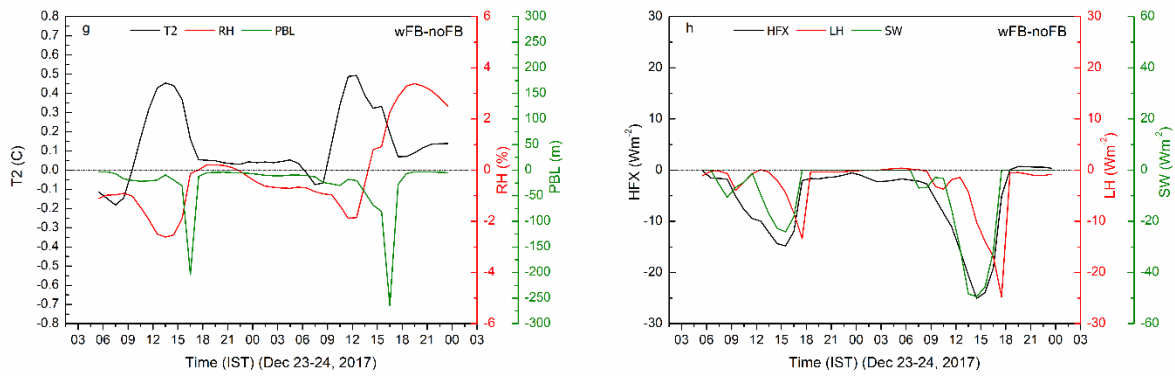
1325 Figure 8 Schematic diagram of Aerosol Radiation Feedback.

1326

1327



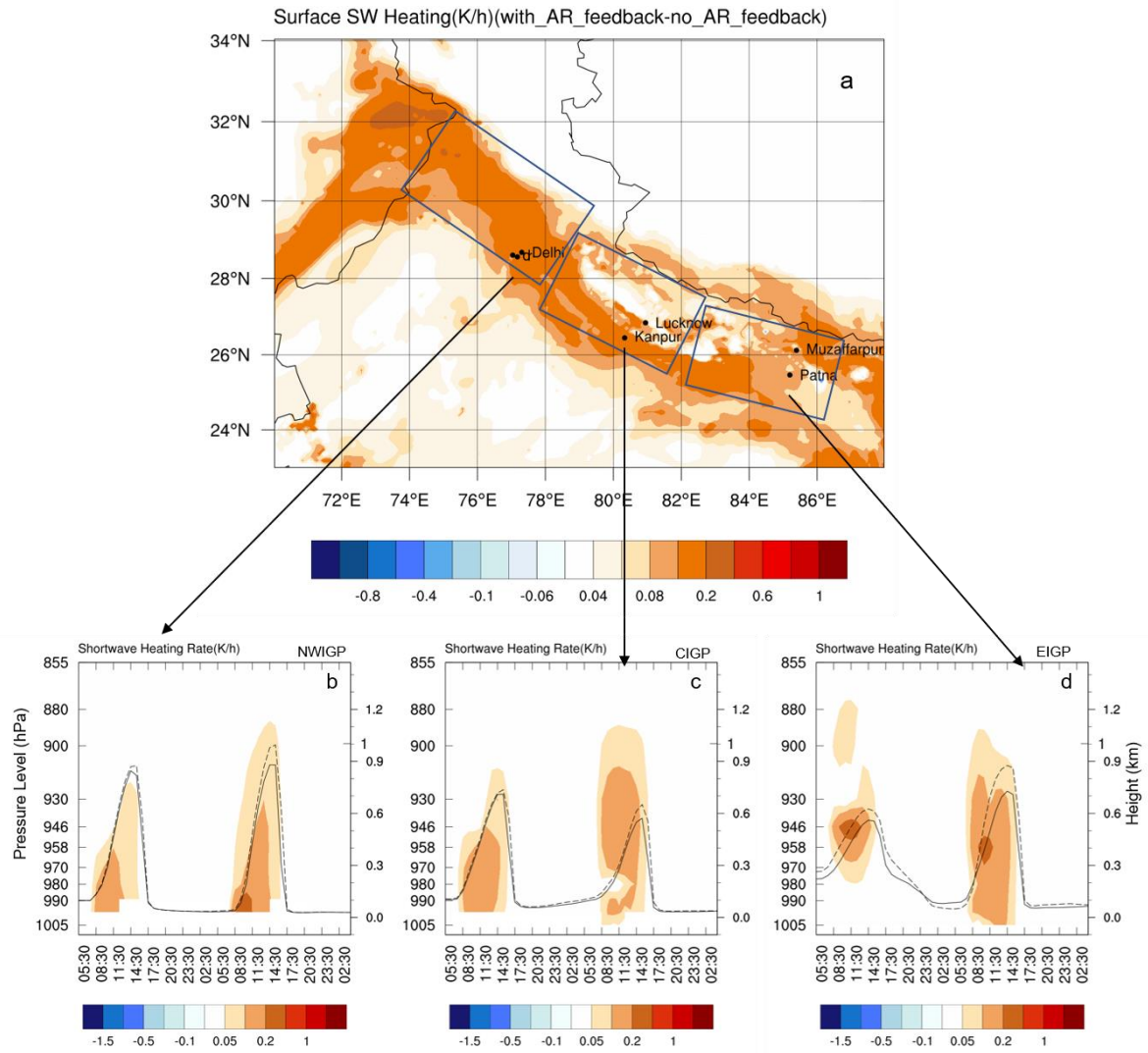
1328



1329

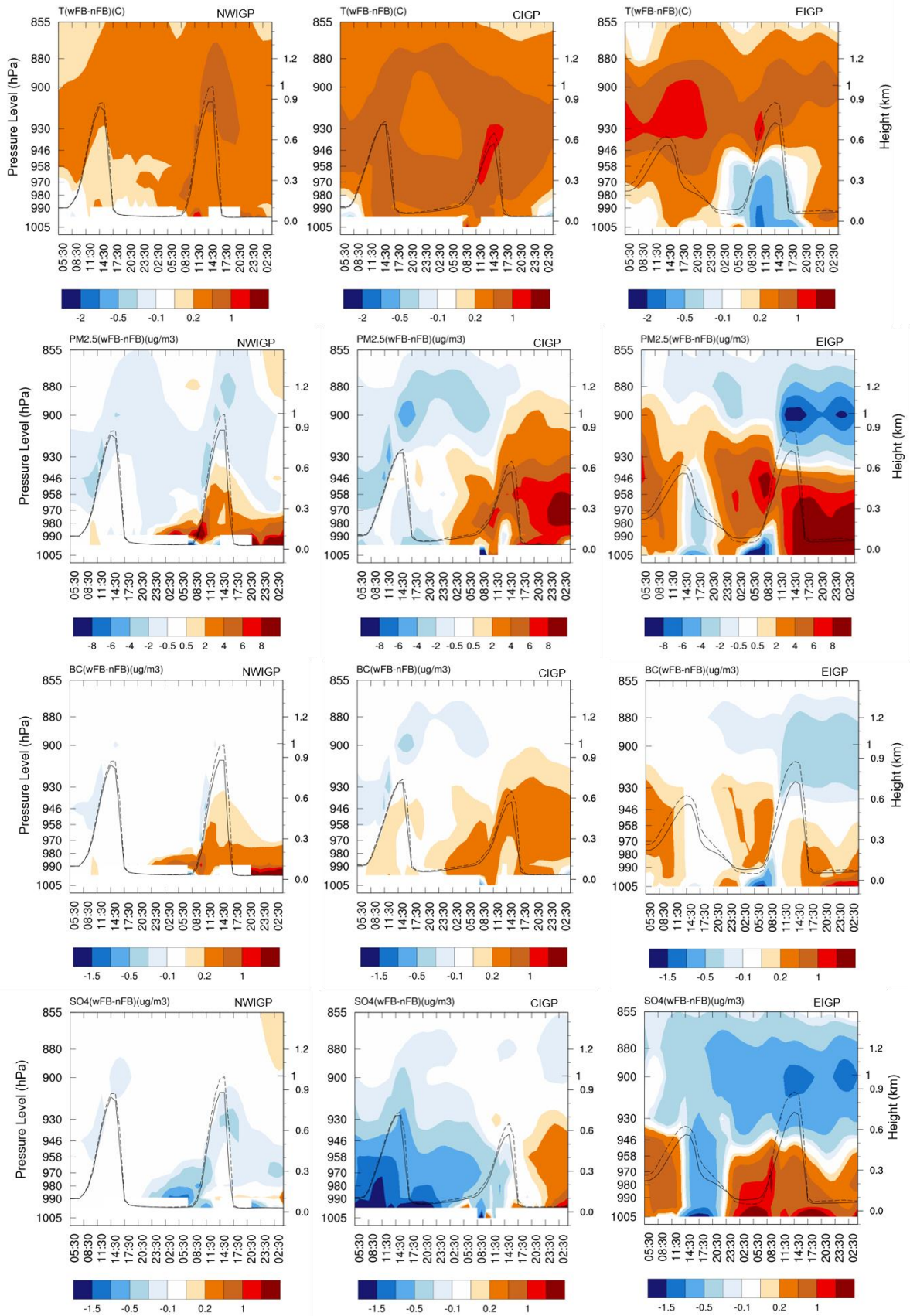
1330 Figure 9 Effect of Aerosol Radiation feedback (wFB-nFB) on (a) PBL height, (b) 2-m temperature, (c)
 1331 2-m relative humidity, (d) surface PM_{2.5}, (e) surface BC and (f) surface SO₄ for December 24 at local
 1332 noon (13:30-15:30 IST). (g) The time series of Δ PBL, Δ T2, and Δ RH; (h) Δ HFX (sensible heat flux),
 1333 Δ LH (latent heat flux), and Δ SWF (downward shortwave flux) over CIGP for December 23 and 24. Δ
 1334 denotes the difference between with and without AR feedback (wFB-nFB).

1335



1336
1337

1338 Figure 10 Differences in shortwave heating rates ($K h^{-1}$) between simulations with and without aerosol
 1339 radiation feedback (a) at the surface, and for pressure-time cross-sections over (b) NWIGP, (c) CIGP.
 1340 And (d) EIGP for December 23 and 24. The solid and dashed lines are the PBL height with and
 1341 without AR feedback respectively. The time is in IST.

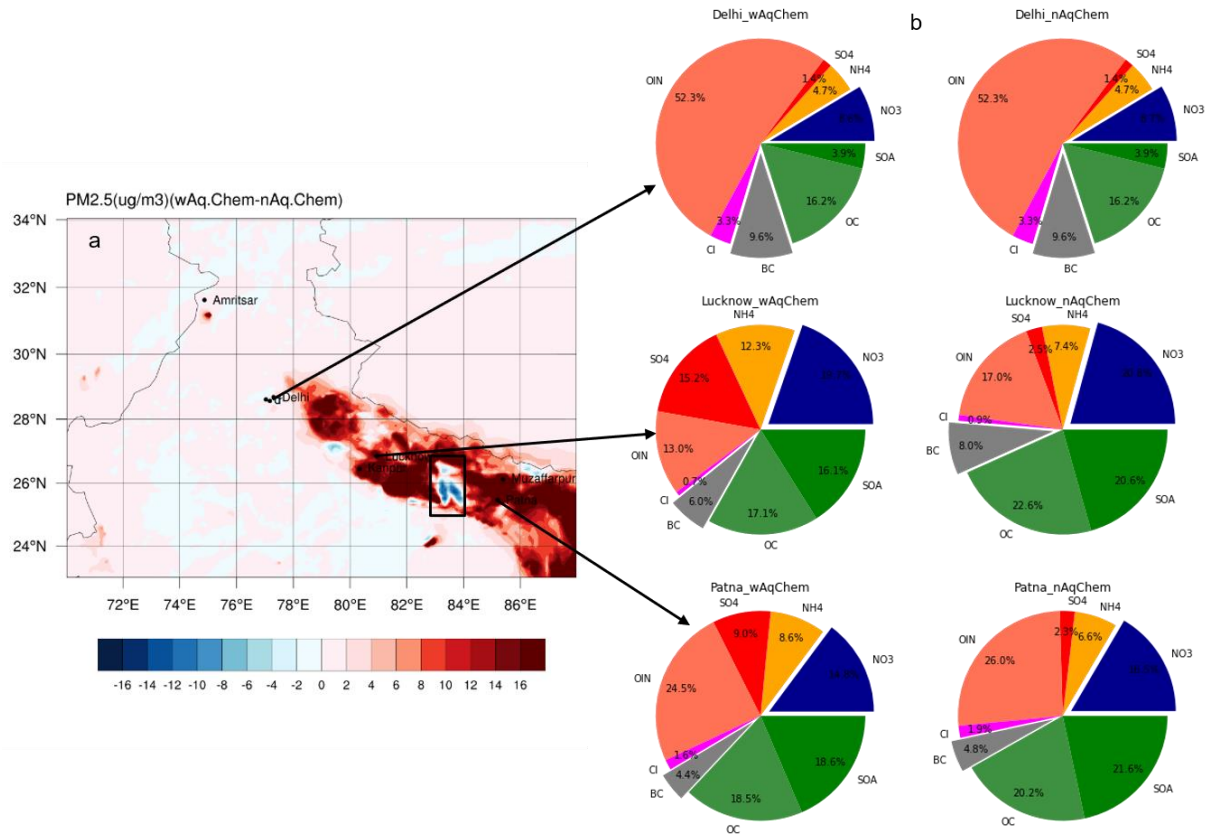


1342

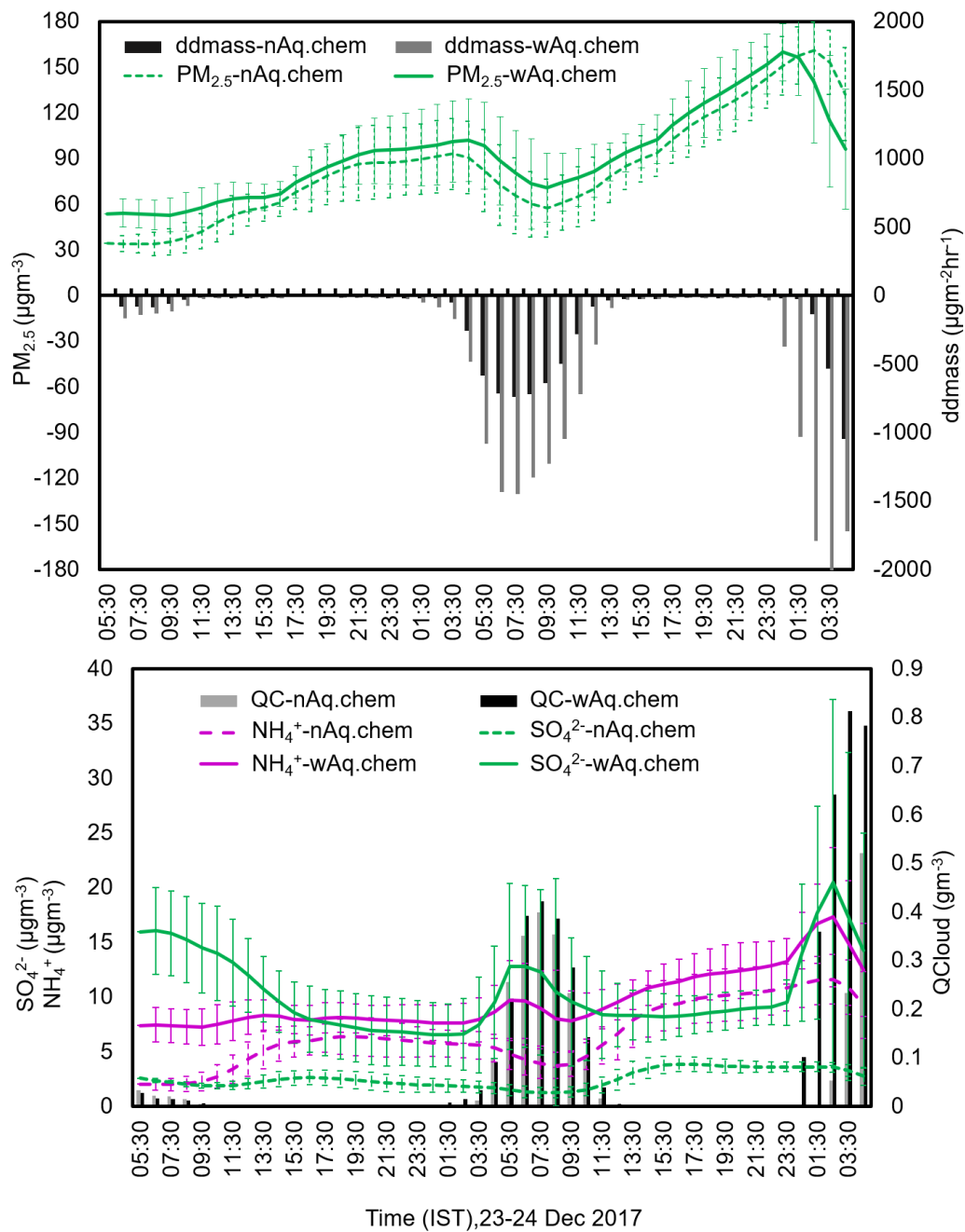
1343

1344

1345 Figure 11 Pressure-time cross-section of the differences in T, PM_{2.5}, BC and SO₄²⁻ between
 1346 simulations with and without the AR feedback for December 23 and 24. The solid and dashed lines
 1347 are the PBL height with and without AR feedback respectively. The time is in IST.
 1348
 1349



1350
 1351 Figure 12 (a) Surface ΔPM_{2.5} (wAq.chem-noAq.chem) and (b) pie charts of PM_{2.5} composition
 1352 distribution for the two cases, with and without Aqueous phase Chemistry for 24 Dec 2017. The
 1353 stations Delhi, Lucknow (LKN), and Patna are representative of NWIGP, CIGP, and EIGP regions
 1354 respectively.
 1355
 1356
 1357

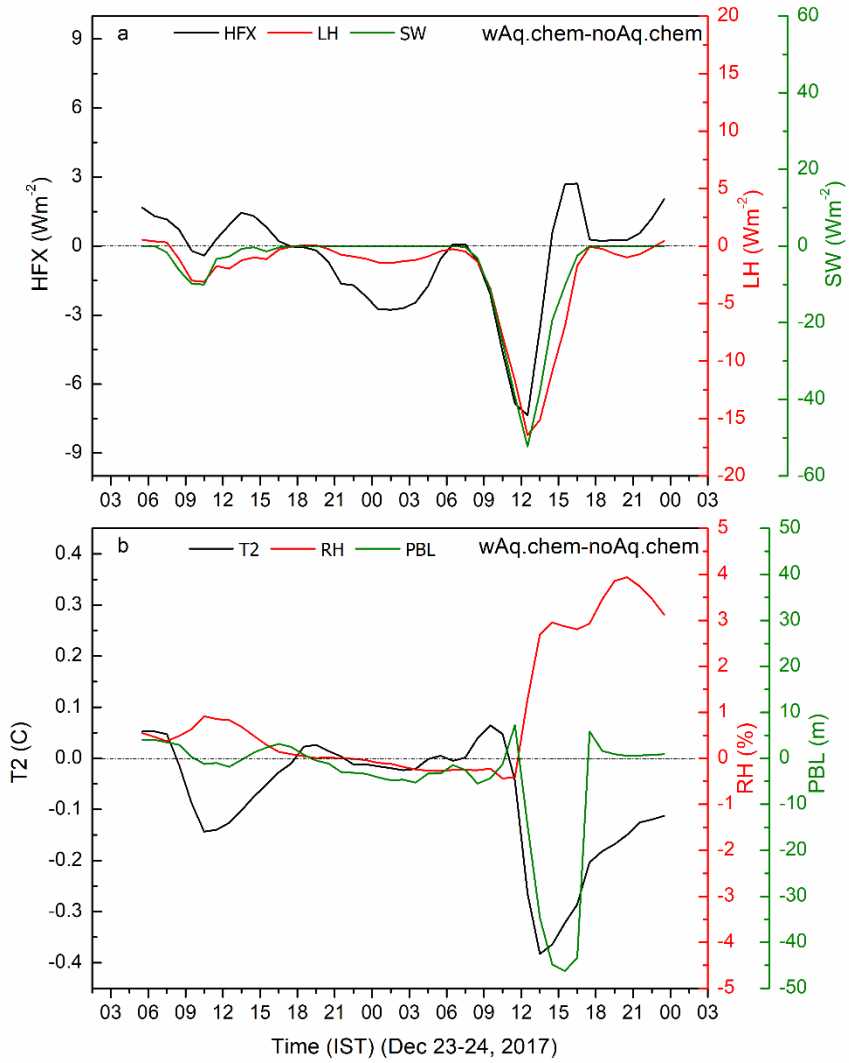


1358

1359 Figure 13 Time series of (a) PM_{2.5} and its dry deposition (ddmass) flux change, (b) SO₄²⁻, NH₄⁺ and
 1360 LWC (QCloud) with and without aqueous phase chemistry included in the model, averaged over the
 1361 region bounded by a black rectangle in Fig. 12, for 23 and 24 December, 2017.

1362

1363



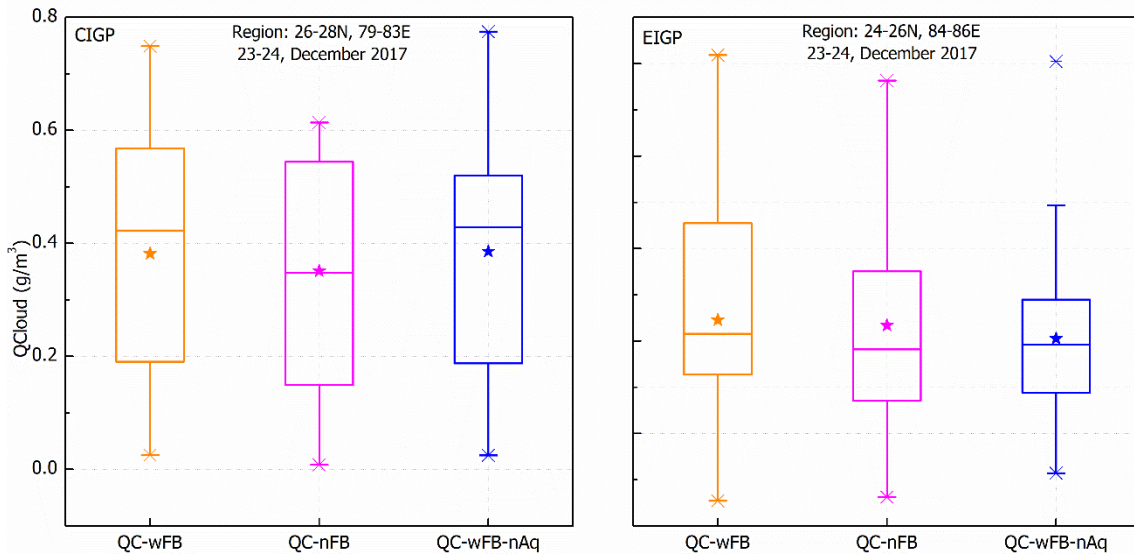
1364

1365

1366 Figure 14 Time series of (a) Δ HFX (sensible heat flux), Δ LH (latent heat flux), and Δ SWF
 1367 (downward shortwave flux); (b) Δ T2, Δ RH, and Δ PBL over CIGP (79E-83E,26N-28N), for
 1368 23 and 24 December, 2017. Δ denotes the difference between with and without aqueous phase
 1369 chemistry.

1370

1371



1372
1373

1374 Figure 15 Averages (stars), medians (horizontal lines), quartiles (boxes), maxima, and minima for
1375 LWC (QCloud) averaged over CIGP (left panel) and EIGP (right panel) for the fog event on 23-24
1376 December 2017. Gold is for the simulation with AR feedback and aqueous chemistry, magenta for the
1377 simulation with no AR feedback but includes aqueous chemistry, and blue for the simulation with AR
1378 feedback but no aqueous chemistry. WRF-Chem does not produce fog in the NWIGP during the study
1379 period.

1380
1381
1382
1383
1384
1385
1386
1387
1388
1389
1390
1391
1392
1393
1394
1395

Table 2: Table showing the start and end time of fog1 on 23-24 December 2017 with LWC for the sensitivity experiments, with AR feedback, no AR feedback and no Aqueous phase chemistry

Fog 1 (December 23-24, 2017)											
	EXP-wFB			EXP-nFB			EXP-nAq.Chem				
	Start time (IST)	End time (IST)	Duration of Fog	Start time (IST)	End time (IST)	Duration of Fog	Start time (IST)	End time (IST)	Duration of Fog		
CIGP	16:30	15:30	23h	18:30	17:30	23h	18:30	15:30	21h		
LWC (g m ⁻³)	0.034	0.036±0.032		0.141±0.154	0.068±0.005		0.184±0.138	0.034 ±0.021			
Kanpur	05:30	13:30	8h	05:30	12:30	7h	05:30	12:30	7h		
LWC (g m ⁻³)	0.334±0.487	0.017		0.458±0.357	0.173±0.071		0.533	0.025±0.0123			
Lucknow	23:30	14:30	15h	00:30	14:30	14h	23:30	14:30	15h		
LWC (g m ⁻³)	0.269±0.145	0.087±0.040		0.232±0.132	0.029±0.024		0.139±0.084	0.025±0.012			
EIGP	21:30	12:30	15h	23:30	10:30	11h	21:30	10:30	13h		
LWC (g m ⁻³)	0.099±0.092	0.007		0.198±0.188	0.084±0.060		0.026±0.008	0.153±0.119			
Patna	00:30	12:30	12h	04:30	10:30	6h	02:30	10:30	8h		
LWC (g m ⁻³)	0.100±0.090	0.007		0.009±0.005	0.038±0.041		0.196±0.198	0.166±0.130			
Muzzafarpur	05:30	11:30	6h	06:30	10:30	4h	06:30	09:30	3h		
LWC (g m ⁻³)	0.112±0.146	0.043±0.057		0.051±0.041	0.003		0.142±0.151	0.157±0.064			

1397

1398 Table 2: Table showing the start time of fog 2 on 24 December 2017 with LWC for the sensitivity
 1399 experiments, with AR feedback, no AR feedback and no Aqueous phase chemistry. Fog2 end time
 1400 could not be noted as simulation ended on 25 December 2017, 00UT (5:30 IST) before fog2
 1401 dissipates.

Fog 2 (December 24, 2017)			
Start time			
(IST)			
	EXP-wFB	EXP-nFB	EXP-nAq.Chem
CIGP	19:30	20:30	21:30
LWC (g m ⁻³)	0.025	0.008±0.007	0.025
Kanpur	21:30	22:30	23:30
LWC (g m ⁻³)	0.041±0.007	0.298±0.218	0.482±0.398
Lucknow	21:30	20:30	00:30
LWC (g m ⁻³)	0.203±0.165	0.005	0.229±0.209
EIGP	00:30	01:30	01:30
LWC (g m ⁻³)	0.024±0.030	0.072±0.088	0.014±0.009
Patna	03:30	03:30	03:30
LWC (g m ⁻³)	0.030±0.046	0.018	0.060
Muzzafarpur	04:30	No fog	No fog
LWC (g m ⁻³)	0.159±0.038		

1402

1403

1404